

Improving Overland Precipitation Retrieval with Brightness Temperature Temporal Variation

YALEI YOU

*Cooperative Institute for Climate and Satellites, Earth System Science Interdisciplinary Center,
University of Maryland, College Park, College Park, Maryland*

CHRISTA PETERS-LIDARD

Hydrological Sciences Laboratory, NASA Goddard Space Flight Center, Greenbelt, Maryland

JOSEPH TURK

Jet Propulsion Laboratory, California Institute of Technology, Pasadena, California

SARAH RINGERUD

Hydrological Sciences Laboratory, NASA Goddard Space Flight Center, Greenbelt, Maryland

SONG YANG

Naval Research Laboratory, Monterey, California

(Manuscript received 27 March 2017, in final form 26 June 2017)

ABSTRACT

Current microwave precipitation retrieval algorithms utilize the instantaneous brightness temperature (TB) to estimate precipitation rate. This study presents a new idea that can be used to improve existing algorithms: using TB temporal variation ΔTB from the microwave radiometer constellation. As a proof of concept, microwave observations from eight polar-orbiting satellites are utilized to derive ΔTB . Results show that ΔTB correlates more strongly with precipitation rate than the instantaneous TB. Particularly, the correlation with precipitation rate improved to -0.6 by using ΔTB over the Rocky Mountains and north of 45°N , while the correlation is only -0.1 by using TB. The underlying reason is that ΔTB largely eliminates the negative influence from snow-covered land, which frequently is misidentified as precipitation. Another reason is that ΔTB is less affected by environmental variation (e.g., temperature, water vapor). Further analysis shows that the magnitude of the correlation between ΔTB and precipitation rate is dependent on the satellite revisit frequency. Finally, it is shown that the retrieval results from ΔTB are superior to that from TB, with the largest improvement in winter. Additionally, the retrieved precipitation rate over snow-covered regions by only using ΔTB at 89 GHz agrees well with the ground radar observations, which opens new opportunities to retrieve precipitation in high latitudes for sensors with the highest frequency at ~ 89 GHz. This study implies that a geostationary microwave radiometer can significantly improve precipitation retrieval performance. It also highlights the importance of maintaining the current passive microwave satellite constellation.

1. Introduction

Many precipitation retrieval algorithms have been successfully developed for several passive microwave sensors, including Special Sensor Microwave Imager (SSM/I) and Special Sensor Microwave Imager/Sounder (SSMIS) (Spencer et al. 1989; Liu and Curry 1992; Petty

1994; Ferraro and Marks 1995; McCollum and Ferraro 2003; Sanò et al. 2013; You et al. 2015), Tropical Rainfall Measuring Mission (TRMM) Microwave Imager (TMI) (Kummerow et al. 2001; Viltard et al. 2006; Wang et al. 2009; Aonashi et al. 2009; Gopalan et al. 2010; Petty and Li 2013; Islam et al. 2015; Ebtehaj et al. 2015), Advanced Microwave Sounding Unit (AMSU) and Microwave Humidity Sounder (MHS) (Staelin and Chen 2000; Grody et al. 2001; Chen and Staelin 2003; Weng et al.

Corresponding author: Yalei You, yyou@umd.edu

DOI: 10.1175/JHM-D-17-0050.1

© 2017 American Meteorological Society. For information regarding reuse of this content and general copyright information, consult the [AMS Copyright Policy](http://www.ametsoc.org/PUBSReuseLicenses) (www.ametsoc.org/PUBSReuseLicenses).

2003; Ferraro et al. 2005; Noh et al. 2006; Surussavadee and Staelin 2008; Laviola and Levizzani 2011; Surussavadee and Staelin 2010; Sanò et al. 2015), Advanced Technology Microwave Sounder (ATMS) (Surussavadee and Staelin 2010; Boukabara et al. 2013; You et al. 2016a), and Advanced Microwave Scanning Radiometer 2 (AMSR-2) (Meyers and Ferraro 2016). In addition to algorithms developed specifically for a certain sensor, there are several more generic algorithms, which are applicable to multiple sensors (Chen and Staelin 2003; Shige et al. 2009; Boukabara et al. 2011; Kummerow et al. 2015; Kidd et al. 2016).

These algorithms differ in the following three aspects. First, a variety of statistical approaches link the brightness temperature (TB) with the precipitation rate, including regression (Ferraro and Marks 1995; Wang et al. 2009; McCollum and Ferraro 2003), Bayes' theorem (Kummerow et al. 2001; Sanò et al. 2013; You et al. 2015), neural network (Sanò et al. 2015; Islam et al. 2015), and shrunk locally linear embedding method (Ebtehaj et al. 2015). Second, the historical precipitation datasets required are derived from several sources, including spaceborne radar [TRMM precipitation radar, Global Precipitation Measurement (GPM) dual frequency precipitation radar, and CloudSat profiling radar] (Wang et al. 2009; Kummerow et al. 2015; Surussavadee and Staelin 2010), ground radar networks (You et al. 2015), or cloud-resolving model output (Kidd et al. 2016). Similarly, the required precipitation profile information can be derived either from cloud-resolving model simulation (Boukabara et al. 2011; Kidd et al. 2016) or from precipitation radar observation (Kummerow et al. 2011). Third, radiative transfer simulations are often indispensable for the more generic algorithms since they need to derive the relationships between TB and precipitation rate for multiple sensors, which often have different channels (Shige et al. 2009; Boukabara et al. 2011; Kummerow et al. 2015). In contrast, radiative transfer models are not necessarily needed when the retrieval algorithm is only for one specific sensor.

These precipitation retrieval algorithms over land seemingly are very different. However, they all share one common feature: using the instantaneous TB in the retrieval process. The primary signature is the TB depression at high-frequency channels (e.g., 85, 166 GHz) due to ice scattering.

To augment existing retrieval algorithms, this study proposes to use TB temporal variation, which is derived from eight polar-orbiting satellites (more details in section 2). It is agreed that the primary precipitation signal over land is the TB depression at high-frequency channels caused by ice scattering. The first motivation of using TB temporal variation is to account for differences in TB

starting values that lead to differences in the TB depression by season. For example, corresponding to the same surface rain rate (e.g., 1 mm h^{-1}), the TB at 89 GHz can decrease 10 K from 300 to 290 K in the summer season, while it also can decrease 10 K from 280 to 270 K in the winter season. When TB is directly used in the retrieval process for these two situations, it will result in a large retrieval error unless ancillary temperature information is incorporated in the retrieval process. We will demonstrate that using TB temporal variation, instead of the instantaneous TB, can largely mitigate this issue. Physically, under moderate to heavy precipitation, the high-frequency channels ($\geq 85 \text{ GHz}$) are surface blind. That is, surface temperature and emissivity variation are of less importance under heavy precipitation scenarios (Ferraro and Marks 1995; You et al. 2011; You and Liu 2012; You et al. 2014). However, the majority of precipitation is light precipitation. This is especially true for the precipitation intensity in the winter season. The background noise can greatly contaminate the rather weak ice scattering signal in winter, which will inevitably result in poor precipitation retrieval performance.

To account for environmental temperature variation, several algorithms incorporate temperature information from reanalysis datasets in the retrieval process (Sanò et al. 2013; You et al. 2015; Kummerow et al. 2015). It is shown that incorporating temperature information improves the precipitation retrieval performance. We will demonstrate that TB temporal variation automatically accounts for the environmental temperature variation, without using the ancillary temperature information.

Another common and serious issue in the precipitation retrieval algorithm development is the cold land surface contamination (e.g., snow-covered land), which is particularly problematic for rainfall/snowfall retrieval in winter because the cold land surface naturally possesses a signal similar to the precipitation signal (You et al. 2015; Chen et al. 2016). For example, snow-covered land pixels are frequently misidentified as precipitating pixels, therefore resulting in a large falsely retrieved precipitation rate. It is possible to screen out these snow-covered land pixels using daily snow-cover maps (Helfrich et al. 2007). However, we show later that there still exist some obvious snow-covered pixels even after screening based on daily snow-cover maps. More importantly, in the winter season, snow accumulation on the ground is prevalent. Screening out these pixels will also discard precipitating pixels, leading to many missing precipitating pixels. We will demonstrate that even if the snow-covered pixel is misidentified as a precipitating pixel, the retrieved precipitation rate by TB temporal variation is close to 0 because that TB temporal variation is close to 0.

The objective of this study is to present a new idea for enhancing precipitation retrievals by using TB temporal variation. We will explain where, when, and why TB temporal variation overcomes some of the limitations of the instantaneous TB for precipitation retrievals. This study is organized as follows. [Section 2](#) describes the passive microwave observations from eight polar-orbiting satellites and the precipitation rate from the ground radar observations. [Section 3](#) shows how to convert TBs from other sensors to GPM Microwave Imager (GMI) frequencies by using several statistical methods, including the simultaneous conical overpass (SCO) technique and principal component analysis (PCA). [Section 4](#) presents the major results from this study. Conclusions and future work are discussed in [section 5](#).

2. Data

This study uses the microwave radiometer observations from eight polar-orbiting satellites, including GMI on board the GPM *Core Observatory* satellite, SSMIS on board Defense Meteorological Satellite Program (DMSP) *F17* and *F18* satellites, ATMS on board *Suomi National Polar-Orbiting Partnership (SNPP)* satellite, and MHS on board *NOAA-18*, *NOAA-19*, *MetOp-A*, and *MetOp-B* satellites. We used all high-frequency channels (≥ 85 GHz) from each sensor. They are 89.0 (V/H), 166.0 (V/H), 183.3 ± 2 (V), and 183.3 ± 7 (V) from GMI; 91.7 (V/H), 150 (H), 183.3 ± 1 (H), 183.3 ± 3 (H), and 183.3 ± 6.6 (H) from SSMIS; 88.2 (V), 165.5 (H), 183.3 ± 1 (H), 183.3 ± 1.8 (H), 183.3 ± 3 (H), 183.3 ± 4.5 (H), and 183.3 ± 7 (H) from ATMS; and 89.0 (V), 157.0 (V), 183.3 ± 1 (H), 183.3 ± 3 (H), and 191.3 (V) from MHS. The letters V and H stand for the vertical and horizontal polarization, respectively. For the cross-track scanning radiometers (ATMS and MHS), the polarization (V/H) is valid only at nadir. This information is summarized in [Table 1](#). Low-frequency channels (e.g., 19 and 37 GHz) from GMI, ATMS, and SSMIS are not considered in this study because they are not available from MHS.

[Table 1](#) also shows the ascending equatorial crossing time (ECT) as of December 2016 for the sun-synchronous orbit satellites. The descending ECT is 12 h earlier than its ascending counterpart. The GPM satellite has a precessing orbit, which means that it overpasses a certain location at varying times throughout the day. Approximately, there is at least one observation in about 3 h for a certain location from these eight satellites' observations. That is, the daily revisit frequency is at least eight times for a certain location over the equatorial region. We show later that over the targeted region, the daily revisit frequency varies from

10 to 16 times, because of the increasing overlap in adjacent swaths as the satellite flies poleward.

All these channels have different footprint resolutions ([Draper et al. 2015](#)). The slightly different frequencies among them (e.g., 89.0 GHz from GMI versus 91.7 GHz from SSMIS) also result in different TBs for the same observations ([Yang et al. 2014](#)). In [section 3](#), we demonstrate a method to bring all these frequencies to a similar resolution. We also convert the TBs from SSMIS, ATMS, and MHS to GMI frequencies by the SCO technique ([Yang et al. 2011](#)) and PCA method (details in [section 3](#)).

The reference precipitation rate data are from the Multi-Radar Multi-Sensor (MRMS) system, which is at 1-km and 2-min spatial and temporal resolution ([Zhang et al. 2016](#)). Collocation between the MRMS precipitation rate and TB is discussed in [section 3](#). Previous work demonstrated that the MRMS precipitation rate is less accurate in mountainous regions due to terrain blockage and in the cold season due to shallow cloud systems ([Chen et al. 2013](#); [Tang et al. 2014](#)). A radar quality index (RQI) is developed to represent the MRMS precipitation data quality ([Zhang et al. 2011](#)). This study only uses the precipitation data with RQI greater than 0.5. This threshold value (0.5) is chosen by considering the trade-off between the sample size and the quality of radar precipitation estimates.

The National Ice Center's Interactive Multisensor Snow and Ice Mapping System (IMS) daily snow-cover map at 24 km resolution ([Helfrich et al. 2007](#)) is used to determine whether a pixel is associated with snow cover on the ground. This study does not distinguish snow-covered land from ice-covered land. We use "snow-covered land" purely for convenience, which includes both snow-covered land and ice-covered land. It is also worth mentioning that the "frost" phenomenon may contribute to false precipitation detection from satellite observations. However, the temporal resolution from these eight satellites ([Table 1](#)) is about 3 h. Considering the shorter frost life cycle, these satellite observations probably cannot account for the frost effect.

Data used in this study are all from March 2014 to December 2016 over the land portion of 25° – 50° N, 130° – 60° W. We choose this period of time since observations from all aforementioned eight satellites are available.

3. Methodology

This section first describes a method to bring all channels from all sensors to a nominal resolution. Then we discuss how to use the SCO technique ([Yang et al. 2011](#)) to obtain the pair of pixels between GMI and the other seven sensors, where the GMI is taken as the reference. Based on the SCO pairs, we show how to use

TABLE 1. Characteristics of each sensor used in this study. The sensors that employed the cross-track scanning scheme are indicated with an asterisk. For the cross-track scanning sensors, the polarization (V/H) is valid only at nadir. The ascending ECT (local time) is as of December 2016 for the sun-synchronous orbit satellites. The GPM satellite has a precessing orbit, which means that it overpasses a certain location at varying times throughout the day.

Satellite name	Radiometer name	Frequency	Frequency	Frequency	Resolution	ECT
GPM	GMI	89.0 (V/H)	166.0 (V/H)	183.3 \pm 3, \pm 7 (V)	6 or 7 km	—
<i>F17</i>	SSMIS	91.7 (V/H)	150.0 (H)	183.3 \pm 1, \pm 3, \pm 6.6 (H)	14 km	1826
<i>F18</i>	SSMIS	91.7 (V/H)	150.0 (H) ^a	183.3 \pm 1, \pm 3, \pm 6.6 (H)	14 km	1845
<i>SNPP</i>	ATMS*	88.2 (V)	165.5 (H)	183.3 \pm 1, \pm 1.8, \pm 3, \pm 4.5, \pm 7 (H)	14–45 km	1331
<i>NOAA-18</i>	MHS*	89.0 (V)	157.0 (V)	183.3 \pm 1, \pm 3 (H); 191.3 (V)	17–40 km	1833
<i>NOAA-19</i>	MHS*	89.0 (V)	157.0 (V)	183.3 \pm 1, \pm 3 (H); 191.3 (V)	17–40 km	1559
<i>MetOp-A</i>	MHS*	89.0 (V)	157.0 (V)	183.3 \pm 1, \pm 3 (H); 191.3 (V)	17–40 km	2129
<i>MetOp-B</i>	MHS*	89.0 (V)	157.0 (V)	183.3 \pm 1, \pm 3 (H); 191.3 (V)	17–40 km	2132

^a The 150-GHz channel on *F18* stopped functioning in February 2012, so it is not used in this study.

the PCA approach to convert TBs from the other seven sensors to GMI channels. Further, we define TB temporal variation. The linear discriminant analysis (LDA) approach for precipitation screening is discussed. Finally, we show how to define the “same location” observations from these eight polar-orbiting satellites.

a. Aggregate the higher resolution TB datasets

The mean footprint resolution of GMI, SSMIS, ATMS, and MHS for the frequencies used in this study is listed in Table 1 (Draper et al. 2015). The GMI has the highest footprint resolution with 7 km at 89.0 GHz and 6 km for higher frequencies (166 and 183.3 GHz). The SSMIS mean footprint resolution is 14 km. The footprint resolution from ATMS and MHS varied from 14 to 45 km from nadir to edge and from 17 to 45 km from nadir to edge, respectively. This study took the SSMIS mean footprint resolution (14 km) as the nominal resolution. The higher footprint resolution from GMI is aggregated to match this resolution, by simply averaging the closest 4 GMI pixels at 89.0 GHz ($14 \times 14/7/7 = 4$) and 6 GMI pixels at 166 and 183.3 GHz ($14 \times 14/6/6 \approx 6$). For ATMS and MHS, we keep their original footprint size. The footprint size of ATMS and MHS at nadir is similar to the nominal resolution. However, the footprint size over the edge is significantly larger. We consider the varying footprint size from the center scan lines and the edge scan lines when converting the TBs to GMI channels in the next section.

For the precipitation rate, we simply average the closest 196 ($14 \times 14 = 196$) 1-km MRMS precipitation rate pixels for each TB observation at the closest time.

Better collocation schemes (e.g., weighted average and Backus–Gilbert method) may further improve the result presented in this study. However, these schemes are much more time consuming than the simple average currently employed in this study. Considering the amount of data from eight satellites,

we choose to utilize the simplest scheme as a proof of concept.

b. Convert TBs from other sensors to TBs at GMI frequencies

After the footprint sizes of these eight sensors are brought to a similar resolution, we convert TBs from the other seven sensors to TBs at GMI channels. The GMI channels are taken as the reference channel because SSMIS, ATMS, and MHS are calibrated against GMI (Berg et al. 2016). From Table 1, it is clear that all other sensors have similar frequencies with those at GMI. The channel similarity between GMI and the other seven sensors enables us to convert TBs from other sensors to TBs at GMI frequencies.

It is worth mentioning that the 150 GHz channel of SSMIS (*F18*) has stopped functioning since February 2012. Therefore, for SSMIS (*F18*), the 150 GHz channel is not used in the TB conversion process. Considering the high correlation between the 150 and 91.7 GHz channels, and between the 150 and 183.3 GHz channels, the absence of the 150 GHz channel likely does not significantly affect the estimated TBs at GMI frequencies.

In the following discussion, we take the GMI and SSMIS (*F17*) as an example to discuss the conversion process. SSMIS (*F17*) frequencies are 91.7 (V/H), 150 (H), 183.3 \pm 1 (H), 183.3 \pm 3 (H), and 183.3 \pm 6.6 (H). This study estimates TBs at 89.0 (V/H), 166 (V/H), 183.3 \pm 3 (V), and 183.3 \pm 7, which are the high-frequency channels from GMI, from the aforementioned TBs from six channels of SSMIS (*F17*). To this end, we first utilize the SCO technique (Yang et al. 2011) to find the SCO pairs between GMI and SSMIS (*F17*). Second, we decompose the GMI TBs from these SCO pairs into principal components (PCs). Third, the SSMIS (*F17*) TBs in these SCO pairs are used to estimate the necessary PCs by a linear regression model. In this study, we select the first five PCs, which account for about 99.6% of total variance.

The coefficients derived from the SCO pairs are then applied to the whole SSMIS (*F17*) data. By doing so, we obtained the estimated PCs from SSMIS (*F17*). These PCs are converted back to TBs at GMI frequencies.

For the sounders (ATMS and MHS), previous work showed that the TBs from edge and center scan lines differ (Weng et al. 2003; Yang et al. 2013; You et al. 2016a). To consider the scanning position effect, for ATMS we group the SCO pairs based on the scan line position into three categories. Specifically, we group the SCO pairs between GMI and ATMS into left-edge SCO pairs (scan position from 1 to 32), center SCO pairs (scan position from 33 to 64), and right-edge SCO pairs (scan position from 65 to 96). Similarly, the SCO pairs between GMI and MHS are grouped into left-edge (1–30), center (31–60), and right-edge (61–90) SCO pairs. Ideally, one would group the SCO pairs to 96 and 90 categories for ATMS and MHS, which fully considered the scanning position effect. However, because of the limited sample size for each scan position, we only group them into three categories. After separating the center and edge SOC pairs, similar procedures between GMI and SSMIS are applied. That is, for each SCO pair (left edge, center, and right edge), we derive different regression coefficients to convert the TBs into TBs at GMI channels.

1) SCO TECHNIQUE

The basic assumption of the SCO technique is that simultaneous measurements at a location from two different sensors at a similar frequency should be highly correlated. This study takes the GMI observations as the reference. Two satellite measurements, one from GMI and the other one from any of the other seven sensors, are called an SCO pair, if the overpass location is less than 1 km and the overpass time is less than 5 min. These threshold values (1 km and 5 min) are chosen by considering the trade-off between the sample size and the SCO pair accuracy.

Over the targeted region from March 2014 to December 2016, there are 39 529 SCO pairs between GMI and SSMIS (*F17*), 37 285 SCO pairs between GMI and SSMIS (*F18*), 16 401 SCO pairs between GMI and ATMS, 12 773 SCO pairs between GMI and MHS (*NOAA-18*), 12 979 SCO pairs between GMI and MHS (*NOAA-19*), 14 011 SCO pairs between GMI and MHS (*MetOp-A*), and 11 576 SCO pairs between GMI and MHS (*MetOp-B*). As discussed in the previous section, the SCO pairs between GMI and each MHS, and between GMI and ATMS, are equally split into three categories based on scan positions.

2) PCA

In this section, we use SCO pairs between GMI and SSMIS (*F17*) as an example to explain the TB conversion

process. The same procedure is applied to SSMIS (*F18*). For ATMS and each MHS, this procedure is applied to the three subcategories based on the scan positions.

Each of the 39 529 SCO pairs between GMI and SSMIS (*F17*) is associated with six GMI TBs [89.0 (V/H), 166 (V/H), 183.3±3 (V), and 183.3±7 (V)] and six SSMIS TBs [91.7 (V/H), 150 (H), 183.3±1 (H), 183.3±3 (H), and 183.3±6.6 (H)]. One possible way to estimate the TBs at GMI frequencies is to treat the GMI frequencies as independent variables. For each GMI channel, we can fit a regression curve with the SSMIS TBs. For example, to estimate the GMI TB at 89.0 GHz (V), we can train a regression curve between GMI TB at 89.0 (V) and SSMIS TB at 91.7 (V). However, we decide not to do so, because the TBs from 89 to 183.3 GHz are highly correlated. Therefore, the following approach is selected.

For SCO pairs between GMI and SSMIS (*F17*), we first decomposed the GMI TBs (six channels) into six PCs (denoted by u_i , $i = 1, 6$). It is noted that the first five PCs account for about 99.6% of total variation. In the following calculation, we only use the first five PCs (i.e., from u_1 to u_5).

The first five PCs are estimated by the TBs from SSMIS (*F17*) at 91.7, 150.0, 183.3±1, 183.3±3, and 183.3±6.6 GHz. For example, for u_1 ,

$$u_1 = a_0 + \sum_{j=1}^6 a_j \times \text{TB}_j, \quad (1)$$

where j is from 1 to 6 for SSMIS, representing the SSMIS channels from 91.7 to 183.3 GHz (see Table 1). The least squares method is used to determine the coefficients from a_0 to a_6 . Similar procedures are used to estimate coefficients from u_2 to u_5 .

The coefficients from a_0 to a_6 , derived from the SCO pairs, are then applied to all the SSMIS (*F17*) observations. By doing so, we convert the TBs from SSMIS into PCs (from u_1 to u_5). Then, TBs at GMI frequencies are reconstructed from the five PCs estimated from SSMIS TBs.

A similar procedure is applied to the other six sensors. By doing so, it is as if we have eight sensors measuring TBs at GMI frequencies, which are 89.0 (V/H) 166.0 (V/H), 183.3±3 (V), and 183.3±7 (V). For convenience, these frequencies are referred to as V89, H89, V166, H166, V186, and V190 from now on.

c. Definition of TB temporal variation

The TB temporal variation ΔTB is defined as

$$\Delta\text{TB} = \text{TB}_{t_0} - \text{TB}_{t_{-1}}, \quad (2)$$

$$\Delta t = t_0 - t_{-1}, \quad (3)$$

where TB_{t_0} is the current TB associated with precipitation and $\text{TB}_{t_{-1}}$ is the immediately preceding TB at

the same location without precipitation. A pixel is judged as a precipitating or nonprecipitating pixel by the LDA approach (Turk et al. 2014; You et al. 2015) (see the following section for more details). The parameter Δt is the time difference between these two observations. From now on, the ΔTB at V89, H89, . . . , V190 will be referred to as $\Delta V89$, $\Delta H89$, . . . , $\Delta V190$ for convenience.

We would like to emphasize that ΔTB is not the difference between two temporally consecutive TB observations. Instead, it is the TB difference between the current TB associated with precipitation and the immediately preceding TB at the same location without precipitation. The physical meaning of this definition is that the immediately preceding TB at the same location without precipitation is taken as the background. By calculating TB temporal variation in this way, we are attempting to extract the current precipitation signal by eliminating the background information. The idea of looking for the previous nonprecipitating scene was also used by Turk et al. (2016) to obtain the emissivities under precipitating scenarios. It is shown that emissivities from 10 to 89 GHz under the precipitating scenarios possibly are obtained by looking backward in time for the most recent TB observations under nonprecipitating conditions at the same location, by using GMI observations.

Clearly, in this definition, we did not consider the environmental variation (e.g., the temperature and water vapor) from t_{-1} to t_0 . The change in environmental conditions from t_{-1} to t_0 can be rather substantial for convection systems, fast-moving fronts, and over cold/warm air boundaries. To consider this information, we need accurate land surface emissivity estimation at 89, 166, and 183.3 GHz. However, the accurate estimation of the emissivity at these frequencies is proven to be very challenging, especially over snow-covered regions (Tian et al. 2015). Therefore, this topic is left for future investigation.

d. LDA

To determine the precipitation status of each pixel, we used the LDA approach. The six TBs are combined into a single discriminant index (DI) for precipitation detection. To put it into perspective, suppose there exist two training databases (i.e., precipitating versus nonprecipitating databases in this study), which contain multivariables \mathbf{x} (i.e., V89, H89, . . . , V190) in each database. According to Wilks (2011) the linear discriminant function to distinguish these two groups is

$$\delta_1 = \mathbf{a}^T \times \mathbf{x}, \quad (4)$$

where T stands for the transpose and \mathbf{a} is the discriminant vector, calculated in the following way:

$$\mathbf{a} = \mathbf{S}_{\text{pool}}^{-1}(\bar{\mathbf{x}}_1 - \bar{\mathbf{x}}_2)$$

$$\mathbf{S}_{\text{pool}} = \frac{n_1 - 1}{n_1 + n_2 - 2} \mathbf{S}_1 + \frac{n_2 - 1}{n_1 + n_2 - 2} \mathbf{S}_2. \quad (5)$$

Bold symbols represent vectors or matrices; $\bar{\mathbf{x}}_i$ and \mathbf{S}_i ($i = 1, 2$) represent the mean vector and covariance of each group, respectively; \mathbf{S}_{pool} is the weighted average of the two sample covariance matrices from these two datasets; and n_1 and n_2 are the samples size in these two groups, respectively.

We choose the DI threshold value for precipitating or nonprecipitating situations, corresponding to the false alarm rate (FAR) at 0.10. Choosing other DI threshold values, corresponding to different FAR values (e.g., 0.05 or 0.15) will only change numerical values in this study. However, the conclusions hold. Previous work showed that including large-scale environmental parameters (e.g., vertical velocity and relative humidity) can improve the precipitation detection performance (You et al. 2015; Behrangi et al. 2015). As a proof-of-concept work, we do not include these parameters in the current study.

e. Definition of the “same location”

The objective of this study is to demonstrate that ΔTB correlates more strongly with precipitation rate and therefore results in improved precipitation retrievals. To this end, we exploited the microwave observations from eight polar-orbiting satellites. To derive TB temporal variation, it is necessary to determine when the observations from different satellites are considered as observations for the same location. This study defines any observation in the same 0.25° latitude–longitude grid box as observations with the same spatial location. We choose the 0.25° grid box because the level-3 merged satellite precipitation products often use this resolution. Choosing a different grid size (e.g., 0.1° or 0.5°) does not affect the major conclusions of this work (e.g., ΔTB correlates more strongly with precipitation rate than the instantaneous TB).

4. Results

a. Two cases of TB time series

This section shows TB time series over two locations. In each case, we first show time series for H89, which is the most sensitive channel to the surface characteristics among the channels used in this study. As a comparison, time series for V190 are also shown, which is less sensitive to surface features and more sensitive to hydrometeors in the air.

Figure 1a shows the time series of H89 from March 2014 to December 2016 over the grid box at 43.5°N ,

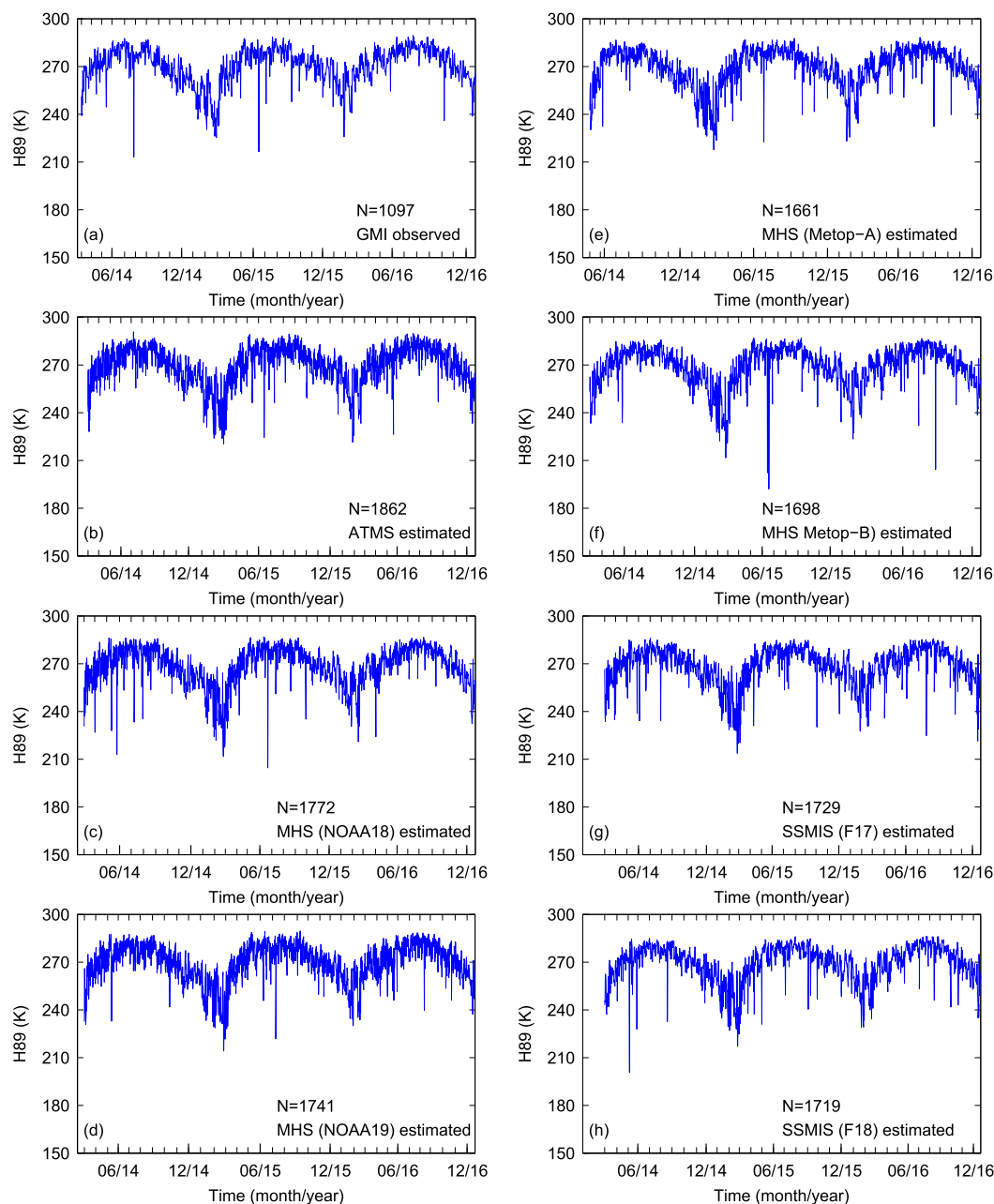


FIG. 1. Time series of H89 from March 2014 to December 2016 over the grid box at 43.5°N, 74°W in New York: (a) observed from GMI and estimated from (b) ATMS, (c) MHS (*NOAA-18*), (d) MHS (*NOAA-19*), (e) MHS (*MetOp-A*), (f) MHS (*MetOp-B*), (g) SSMIS (*F17*), and (h) SSMIS (*F18*).

74°W in New York. In Figs. 1b–h, TB at H89 is estimated from ATMS, MHS (*NOAA-18*), MHS (*NOAA-19*), MHS (*MetOp-A*), MHS (*MetOp-B*), SSMIS (*F17*), and SSMIS (*F18*), respectively. The sample number from each sensor at this location is also shown in Fig. 1 (e.g., $N = 1097$ from GMI in Fig. 1a).

First, it is clear that H89 from these eight sensors have similar seasonal variation. The dynamical range also is similar. The cold TBs in the winter season of 2015/16

(December–February) are obvious from each sensor. The daily snow-cover map shows that the majority of these pixels are associated with snow-covered land. These pixels are frequently misidentified as precipitation pixels, which leads to large false precipitation estimation. We show later that using TB temporal variation can largely mitigate the snow-covered land contamination. The time series from each sensor are not identical because each sensor overpasses this location at different times.

Second, using all these observations from eight sensors significantly increases the revisit frequency for this location, which is essential to calculate TB temporal variation. We demonstrate later that the shorter the revisit time, the better the correlation between TB temporal variation and precipitation intensity is, which is especially the case over the rapidly changing land surfaces (e.g., snow-covered land).

The time series of V190 in the same period of time at the same location are also analyzed. As expected, V190 has a much smaller seasonal variation (figure not shown because of space limitations), compared with that at H89 (Fig. 1a), because it is less affected by the surface characteristics than H89. On the other hand, similar to the H89, V190 from different sensors behaves very similarly. Figures 2a and 2b show the combined time series of H89 and V190 at this location, respectively. There are no obvious outliers observed when pooling data from all eight sensors together. It indicates that our method can effectively convert TBs from other sensors to GMI channels. Similar characteristics are noticed from other channels (V89, V166, H166, and V186).

Another case over the grid box at 30.5°N, 86°W in Florida also is demonstrated in Figs. 2c and 2d. At this location, the seasonal variation is much less pronounced for both H89 and V190. In particular, V190 has no noticeable seasonal variation (Fig. 2d). Again, there are no obvious outliers observed in Figs. 2c and 2d, indicating that our method effectively converted TBs from other sensors to GMI channels. In the next several sections, we show that TB temporal variation in this location can significantly alleviate environmental variations and can therefore lead to a better correlation between precipitation intensity and TB temporal variation, compared with the instantaneous TB.

It is worth mentioning that long spikes (i.e., cold TBs) in Fig. 2 generally correspond to the precipitation occurrence. However, the snow-covered land also can lead to cold TBs (e.g., the spikes in January and February over the grid box at 43.5°N, 74°W in New York in Fig. 2a). These pixels often are falsely identified as precipitation pixels. We show later that TB temporal variation is almost insensitive to the contamination from these snow-covered pixels.

To summarize, this section demonstrates that the SCO and PCA approaches can effectively convert TBs from other sensors to GMI channels.

b. Correlation between TB temporal variation and precipitation intensity

Figure 3 shows the correlation coefficients of precipitation intensity with the instantaneous TB

(V89, H89, . . . , V190) and Δ TB at the corresponding channel (Δ V89, Δ H89, . . . , Δ V190). It is immediately clear that using Δ TB improves the correlation with the precipitation intensity for all channels, which is particularly evident over regions with cold surfaces (e.g., Rocky Mountains and north of 45°N). For example, the correlation between V89 and precipitation rate (Fig. 3a) over the Rocky Mountains and northeast of the targeted region is about 0.1. This positive correlation is a false signal, which does not mean that V89 increases due to precipitation effect. Instead, we demonstrate below that this positive correlation is caused by misidentified snow-covered pixels. In contrast, Δ V89 dramatically improves the correlation with the precipitation rate. Specifically, the correlation over the aforementioned two regions improved to about -0.6 . The negative correlation basically means that the precipitation results in a TB depression at V89 as a result of the ice scattering effect, which has been realized from the very beginning of passive microwave observations over land (Spencer et al. 1989). We demonstrate below that the better correlation from Δ V89 is because Δ V89 almost eliminates the cold surface contamination, which is often misidentified as precipitation signal.

The superiority of Δ TB is further demonstrated by the scatterplot in Fig. 4, which shows the correlation coefficients from the instantaneous TB and the corresponding Δ TB. For example, the x axis in Fig. 4a represents the correlation between Δ V89 and precipitation rate, and the y axis represents the correlation between V89 itself and precipitation rate. For all six channels, the magnitude of the correlation coefficient from Δ TB is larger than that from TB over about 92.0% of grid boxes for all channels.

For the rest grid boxes (about 8.0%), Δ TB has a slightly lower correlation to MRMS precipitation rate than the instantaneous TB. Further analysis shows that these grid boxes are all located in coastal regions. Coastal pixels cause problems for Δ TB computations that are not reflected in the instantaneous TB. For example, pixel A from GMI in a coastal grid box is judged as a raining pixel. To compute Δ H89 for this pixel, the immediately preceding TB at this 0.25° grid box is from SSMIS (F17) (referred to as pixel B). Although pixel B is in the same grid box as pixel A, pixel B is contaminated by the ocean surface; therefore, H89 is much lower due to the low ocean surface emissivity. Using pixel B's information, Δ H89 is indirectly contaminated by the ocean surface. On the other hand, the ocean surface contamination from pixel B has no influence at all on pixel A when directly using TB. This problem can be rectified using high-resolution land-water masks, and this work is left as a future refinement to the proof of concept demonstrated here.

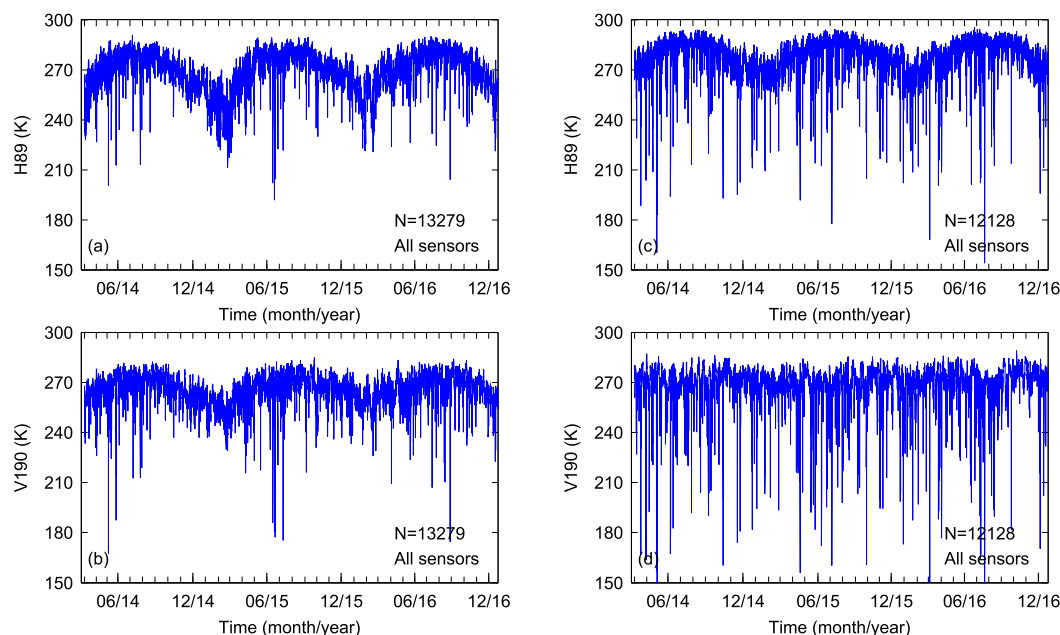


FIG. 2. (a) Time series of H89 from March 2014 to December 2016 over the grid box at 43.5°N , 74°W in New York, from all sensors. (b) As in (a), but for V190. (c) As in (a), but over the grid box at 30.5°N , 86°W in Florida. (d) As in (b), but over the grid box at 30.5°N , 86°W in Florida.

1) SNOW-COVERED LAND EFFECT

This section uses the data from the previously mentioned grid box at 43.5°N , 74°W in New York to explain why ΔTB correlates much more strongly with precipitation rate than TB.

As shown previously, this location frequently experiences snow accumulation over the ground in the winter season. The correlation between ΔH89 and precipitation rate is -0.66 (Fig. 5a). On the other hand, H89 correlates with precipitation rate very poorly with a correlation coefficient at -0.27 (Fig. 5b).

Observations can be further divided into non-snow-covered data and snow-covered data. For the non-snow-covered data, the correlation between ΔH89 and precipitation rate is improved slightly from -0.66 to -0.71 (Fig. 5c). However, the correlation between H89 and precipitation rate is dramatically improved from -0.27 to -0.57 (Fig. 5d). The much-improved correlation from H89 itself by using the non-snow-covered data is clearly due to screening out the snow-covered pixels. In fact, this issue is well known, and precipitation retrieval algorithms often include snow-cover screening steps (Ferraro et al. 1998; Kummerow et al. 2001; You et al. 2016b). However, it is noted that even after using the daily snow-cover map to screen out the possible snow-covered pixels, there still exist some pixels with snow-cover contamination (Fig. 5d, pixels with no precipitation

and H89 about 250 K). In contrast, the snow-covered contamination is largely eliminated when using ΔH89 (Fig. 5c). This result further demonstrates the added value of ΔTB relative to the instantaneous TB.

For pixels over snow-covered land, the correlation between ΔH89 and precipitation is -0.34 (Fig. 5e), while there is weak positive correlation at 0.08 between H89 and precipitation rate (Fig. 5f). The positive correlation is caused by the falsely identified precipitation pixels over snow-covered land with very cold TBs. It is worth mentioning that one cannot simply discard the pixels over the snow-covered land. By doing so, pixels over snow-covered land with precipitation also are discarded and will lead to missing precipitation pixels.

The red, green, and magenta curves in Figs. 5a–f are regression lines derived from the least squares approach. Figure 5g shows that the regression curves from the entire dataset (red line), non-snow-covered subset (green line), and snow-covered subset (magenta line) are almost identical, which essentially means that the relationship between ΔH89 and precipitation rate is largely independent of the snow-cover accumulation on the ground. In contrast, the snow-covered pixels can alter the relation between H89 and precipitation rate, as indicated by three very different regression curves in Fig. 5h.

The relative independence of ΔH89 to the snow-covered contamination implies that the sensors with the highest available frequency at $\sim 89\text{ GHz}$ (e.g.,

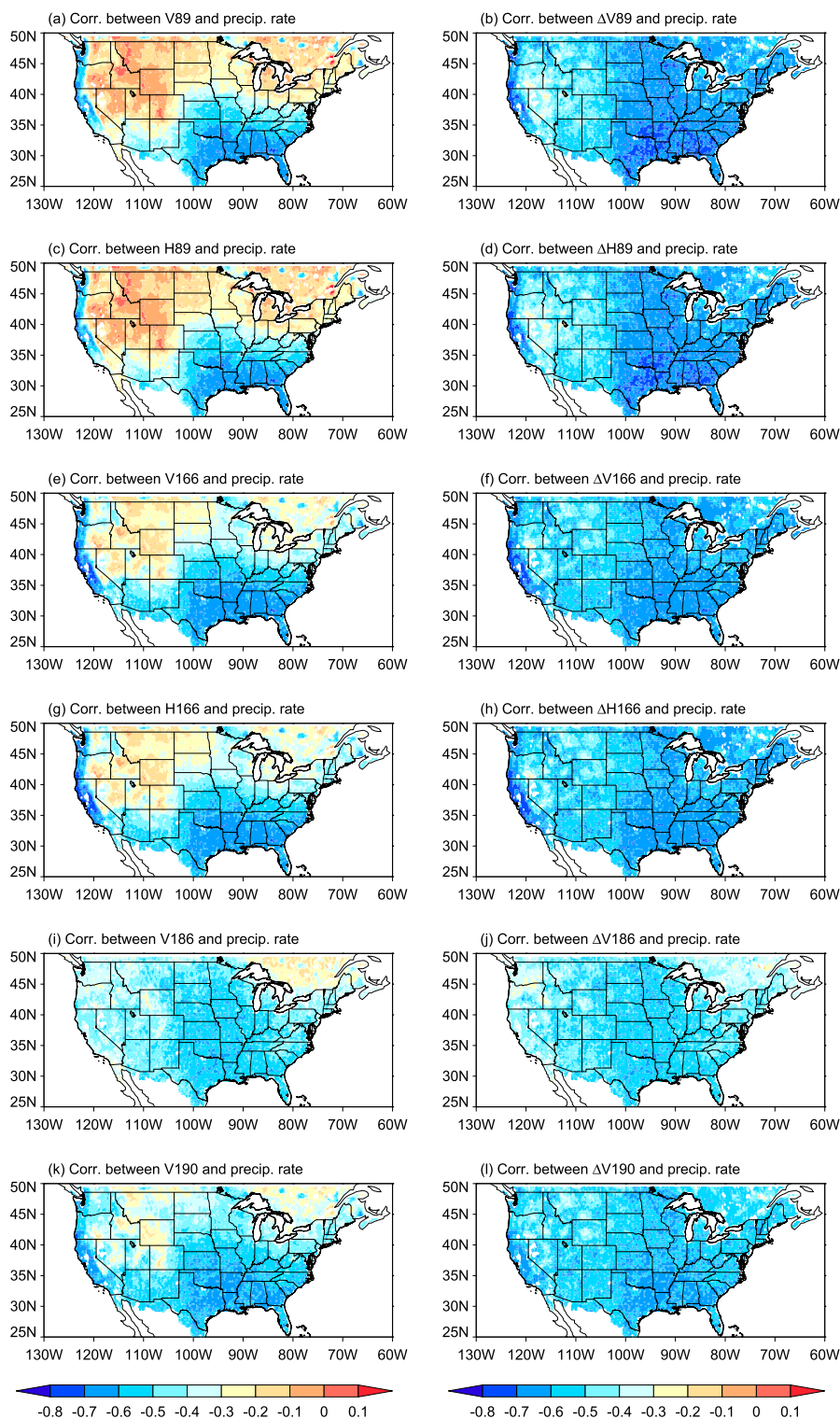


FIG. 3. (left) Correlation between the instantaneous TB and precipitation rate. (right) Correlation between precipitation rate and ΔTB at the corresponding channel.

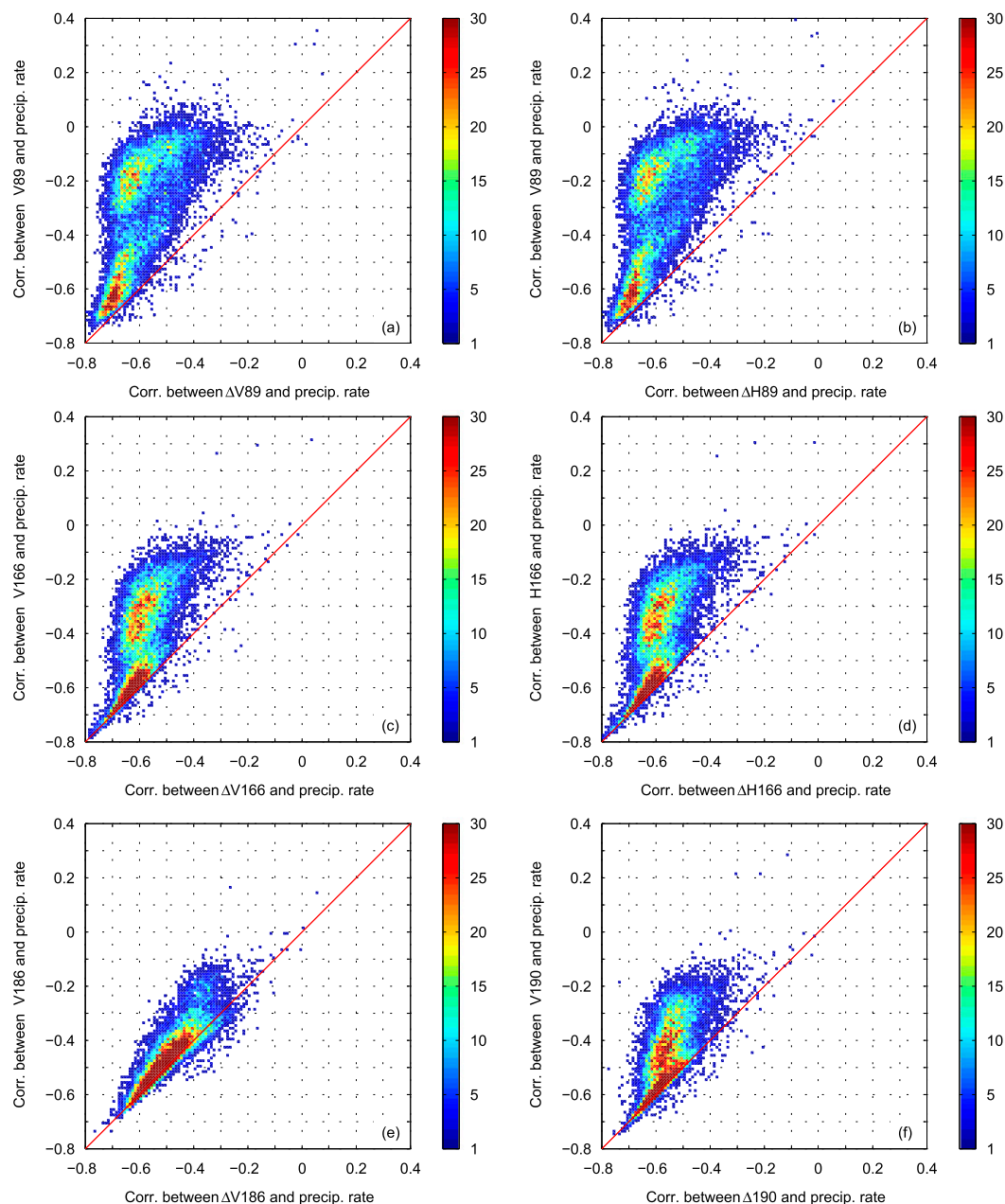


FIG. 4. (a) Scatterplot based on correlation between $\Delta V89$ and precipitation rate (x axis), and correlation between $V89$ and precipitation rate (y axis). (b) As in (a), but for H89. (c) As in (a), but for V166. (d) As in (a), but for H166. (e) As in (a), but for V186. (f) As in (a), but for V190.

AMSU-A and AMSR-2) can be used to retrieve precipitation over cold surfaces. This is in contrast to the generally accepted practice that these sensors have poor capability for precipitation retrieval in the winter season due to the cold surface contamination (Fig. 5f). Our analysis shows that using ΔTB at ~ 89 GHz to retrieve precipitation over cold land surfaces in the winter season overcomes these limitations from the satellite constellation perspective.

We further analyzed the snow-covered land contamination at V190 (Fig. 6). Similarly, $\Delta V190$ outperforms V190, as indicated by the larger correlation coefficient. As expected, V190 is less affected by the surface characteristics. However, there still exist noticeable differences among these three regression curves from all data, non-snow-covered data, and snow-covered data (Fig. 6h), while regression curves are almost identical based on $\Delta V190$ (Fig. 6g).

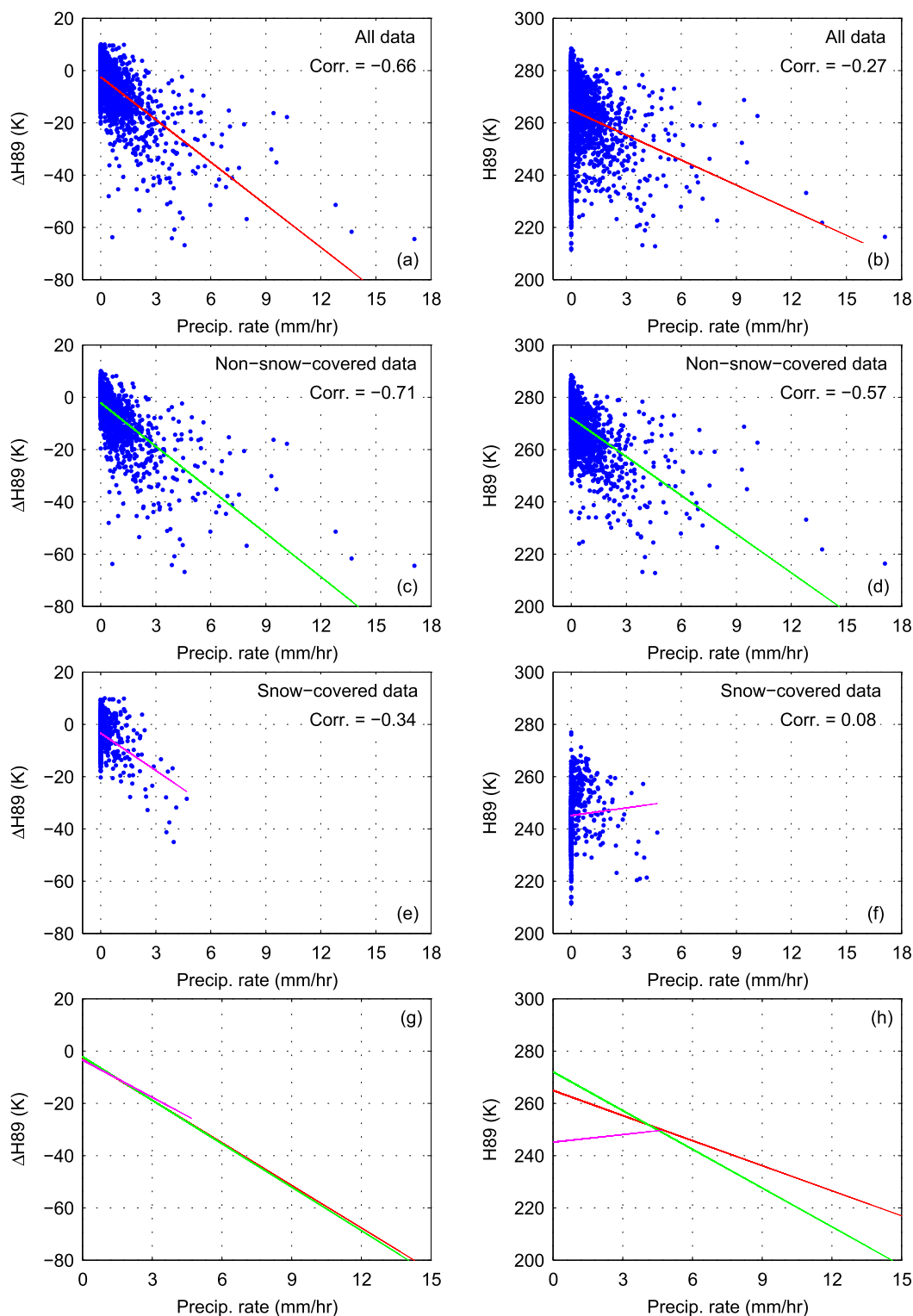


FIG. 5. Case study over the grid box at 43.5°N, 74°W in New York. (a) Scatterplot between precipitation rate and $\Delta H89$. (b) Scatterplot between precipitation rate and H89. (c) As in (a), but only the non-snow-covered data are used. (d) As in (b), but that only the non-snow-covered data are used. (e) As in (a), but only the snow-covered data are used. (f) As in (b), but only the snow-covered data are used. (g) The regression curves from (a), (c), and (e). (h) The regression curves from (b), (d), and (f).

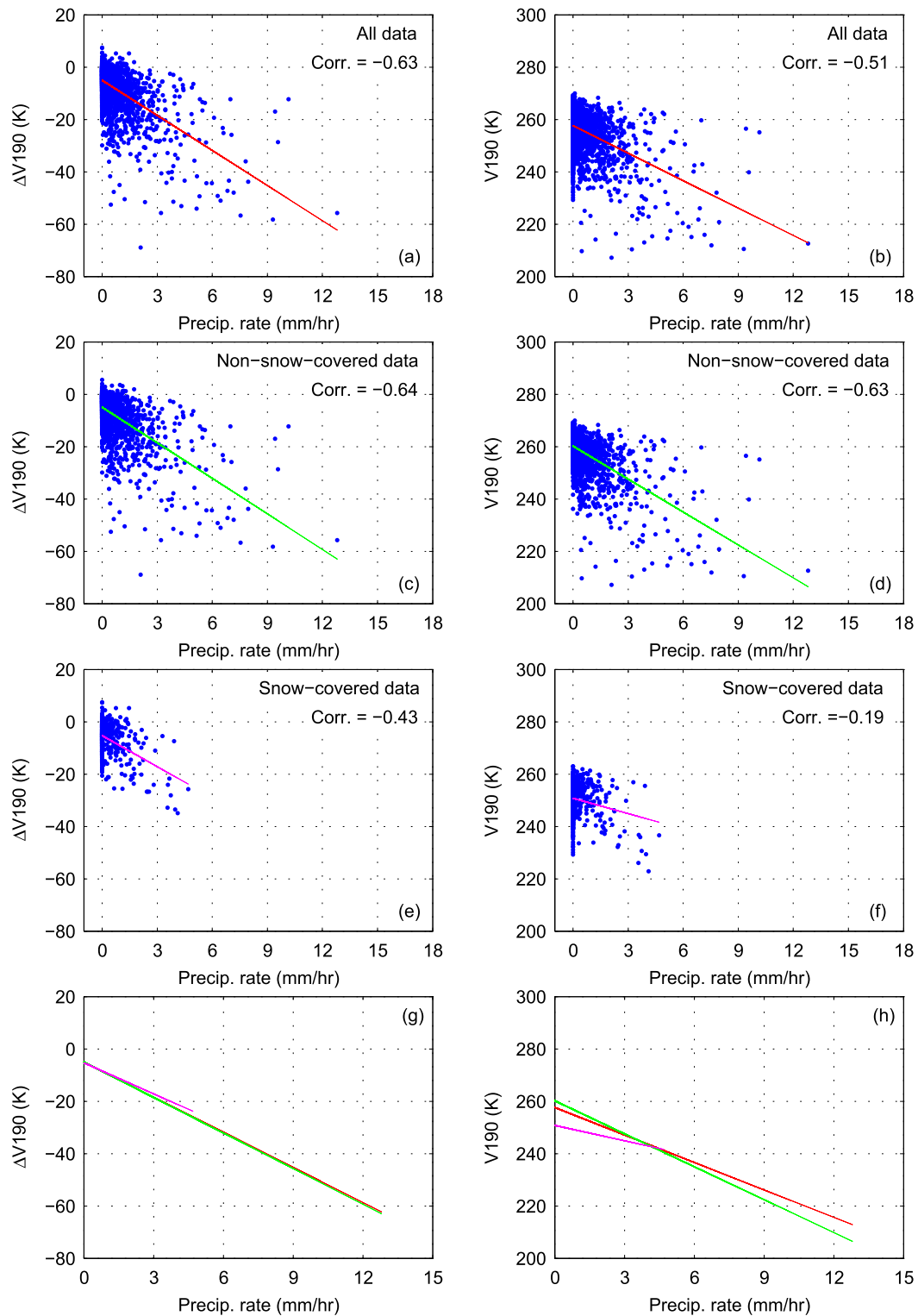


FIG. 6. As in Fig. 5, but for V190.

2) ENVIRONMENTAL VARIATION EFFECT

This section focuses on data from the grid box at 30.5°N, 86°W in Florida to explain why even in a rarely snow-covered region, ΔTB still adds information relative to the instantaneous TB.

To demonstrate the effects of environmental (e.g., temperature, humidity) variation, we analyze the relationships between precipitation rate and ΔTB , and between precipitation rate and TB, in winter and summer. The correlation between $\Delta H89$ and precipitation rate (Fig. 7a) is -0.74 , which is only slightly larger than that between $H89$ and precipitation rate at -0.69 (Fig. 7b). It is noted that data in both winter and summer are used in these two figures (Figs. 7a,b). When the data are divided into summer and winter subsets, similar correlations with precipitation rate based on either $H89$ or $\Delta H89$ are found (cf. Figs. 7c and 7d and Figs. 7e and 7f).

As stated in the introduction, the problem is that the starting values from which $H89$ decrease are different in summer and winter. In the summer season, $H89$ decreased from about 282 K (green curve in Fig. 7d), as opposed to 268 K in winter (magenta curve in Fig. 7f). However, $\Delta H89$ is almost unaffected by environmental variation from summer to winter. The $\Delta H89$ in both seasons decreases from about -2 K. Figure 7g shows that these three curves based on both winter and summer data, or based on summer or winter only data, are almost identical by using $\Delta H89$. On the contrary, the relations between $H89$ and precipitation rate using data in winter and summer are quite different (Fig. 7f). For V190, environmental variation has much less influence, compared with $H89$ (not shown because of space limitations). However, it is found that $\Delta V190$ is less affected by the seasonal environmental variation, compared with V190.

In summary, this section shows that ΔTB correlates more strongly with precipitation rate than the instantaneous TB. This, combined with the analysis in the previous section, shows that ΔTB is much less affected by snow-covered land contamination, and also less sensitive to environmental variation. These two factors account for the superior performance of ΔTB .

c. Correlation seasonal variation

This section analyzes the seasonal variation of the correlation between TBs themselves and precipitation rate, and between ΔTB at the corresponding channel and the precipitation rate. Figures are not shown because of space limitations.

In spring, the largest correlation improvement is observed over the Rocky Mountain region and areas

north of 45°N. This improvement is more obvious for V89 and H89. Similar features are observed in fall. In summer, the correlation improves very little by using ΔTB . As mentioned previously, the primary reason why ΔTB improves the correlation is because of the mitigation of land surface contamination. In summer, there is almost no snow accumulation in the targeted region. Therefore, we did not observe much improvement. However, the snow-covered land contamination remains an issue in the higher-latitude region even in summer (e.g., Alaska). Therefore, ΔTB is expected to perform better in the higher-latitude regions even in the summer season.

The largest improvement is observed in the winter season, when the snow accumulation on the ground is prevalent. In this situation, ΔTB can significantly alleviate surface contamination and can therefore result in a much stronger correlation with the precipitation rate. Obviously, there still exist false positive correlations in Montana, Wyoming, North Dakota, and South Dakota, even using ΔTB . The misidentified snow-covered pixels cause this problem. To illustrate this point, we choose the grid box at 47°N, 114°W at Missoula, Montana, where one of the NEXRAD radars operates.

Figure 8a shows that the correlation between $H89$ and precipitation rate is 0.15. It is worth mentioning that almost all the pixels in this location in winter are associated with snow accumulation on the ground, as determined by the IMS daily snow-cover map. The positive correlation is clearly caused by the misidentified snow-covered pixels, which are associated with no precipitation. Using $\Delta H89$ can mitigate the snow-covered pixels' influence to some extent, as indicated by the smaller positive correlation at 0.04 (Fig. 8b). By only using the pixels with the time difference less than 24 h ($\Delta t < 24$), the correlation between $\Delta H89$ and precipitation rate is improved to -0.19 (Fig. 8c). It is further improved to -0.34 when only using data with the time difference less than 6 h ($\Delta t < 6$; Fig. 8d). This phenomenon indicates that $\Delta H89$ is less affected by snow-cover contamination with a shorter time difference between the current precipitating pixels and the immediately preceding nonprecipitating pixels at the same location. In other words, $\Delta H89$ contains more signal from the current precipitation, not the contamination signal, when the time difference is shorter (e.g., the surface emissivity variation due to snowpack melt and refreezing, or new snow accumulation on the ground). Another possible reason is that with a shorter time difference, the environmental parameters (e.g., temperature profiles) between t_0 and t_{-1} are more similar. This case study demonstrates that even ΔTB is strongly affected by snow-covered pixels when precipitation intensity is light (less than 3 mm h^{-1} in this case).

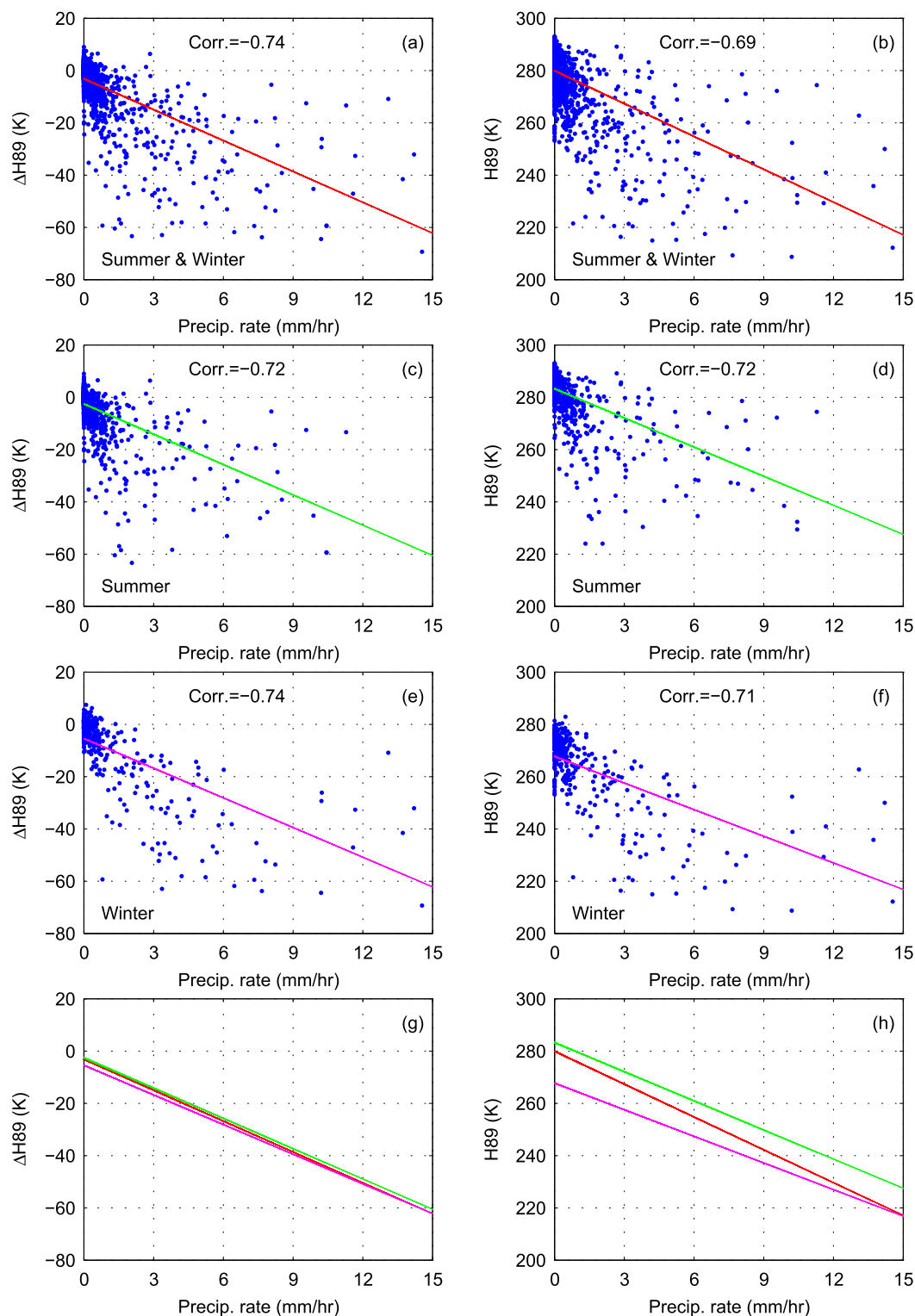


FIG. 7. Case study over the grid box at 30.5°N, 86°W in Florida. (a) Scatterplot between precipitation rate and $\Delta H89$. (b) Scatterplot between precipitation rate and H89. (c) As in (a), but only the data in summer are used. (d) As in (b), but only the data in summer are used. (e) As in (a), but only the data in winter are used. (f) As in (b), but only the data in winter are used. (g) The regression curves from (a), (c), and (e). (h) The regression curves from (b), (d), and (f).

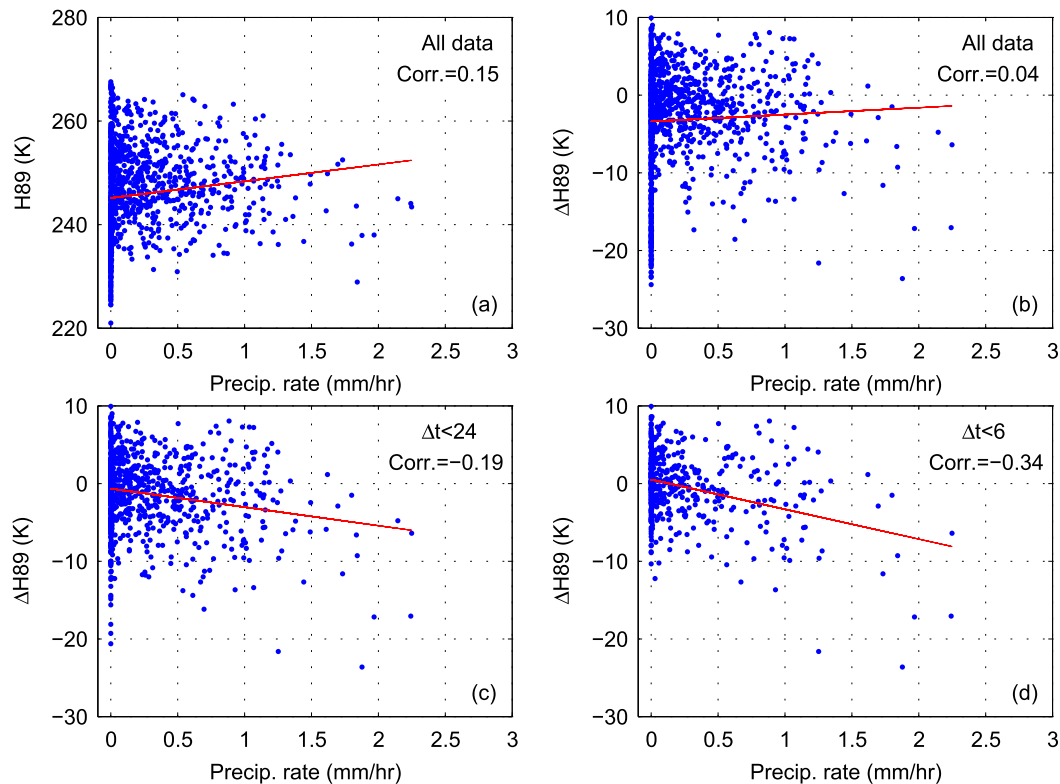


FIG. 8. Case study over the grid box at 47°N, 114°W at Missoula, Montana. (a) Scatterplot between precipitation rate and H89. (b) Scatterplot between precipitation rate and $\Delta H89$. (c) As in (b), but only the data with $\Delta t < 24$ h is used. (d) As in (b), but only the data with $\Delta t < 6$ h is used.

d. Time difference influence

The objective of this study is to show ΔTB is better correlated with the precipitation rate than the instantaneous TB. Observations from a potential geostationary microwave radiometer (Lambrijsen et al. 2006; Gaier et al. 2016) would be ideally suited for this approach because of the much higher temporal resolution and fixed time interval between the two observations. However, a spaceborne geostationary microwave radiometer is currently not available. Therefore, we must exploit observations from eight polar-orbiting satellites. By doing this, the Δt defined in Eq. (3) is highly variable. We have already demonstrated in the previous section (Fig. 8) that the correlation between $\Delta H89$ and precipitation rate is dependent on the Δt variation. This section further demonstrates the effect of variable Δt on the correlation between ΔTB and precipitation rate.

Table 2 shows the observation number from each sensor from March 2014 to December 2016 in the targeted region. GMI has the smallest sample size with 19.01 million observations, due to the relatively narrow swath coverage. For the other seven sensors, each has about 30 million observations. On average, the revisit

frequency for any sensor is less than 2 times daily. By combining observations from all eight sensors, the revisit frequency is greatly improved. The revisit frequency is improved to 10–16 times daily, depending on the latitude (Fig. 9). A much more frequent revisit for a certain location leads to a much shorter Δt , which is critical for correlation between ΔTB and precipitation rate.

Figure 10 shows the histogram of the time difference (i.e., Δt) from eight sensors and from GMI only. Again,

TABLE 2. Sample size of each sensor from March 2014 to December 2016 at 0.25° resolution in the targeted region (25°–50°N, 130°–60°W).

Satellite name	Radiometer name	No. of obs. (million)	Percentage (%)
GPM	GMI	19.01	8.25
F17	SSMIS	32.76	14.21
F18	SSMIS	30.22	13.11
SNPP	ATMS	30.27	13.13
NOAA-18	MHS	28.95	12.56
NOAA-19	MHS	29.72	12.89
MetOp-A	MHS	29.76	12.91
MetOp-B	MHS	29.83	12.94

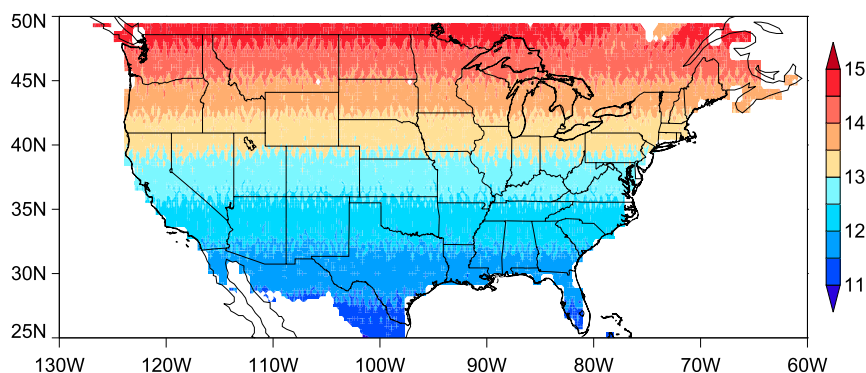


FIG. 9. Daily revisit frequency from eight sensors for each 0.25° grid box based on observations from March 2014 to December 2016.

we emphasize that Δt is not the time difference between two consecutive observations. It is the time difference between the current precipitating pixel and the immediately preceding nonprecipitating pixel at the same location. With the observations from eight sensors (Fig. 10a), the vast majority of Δt (91.10%) are less than 24 h. It basically means that for 91.10% of precipitating pixels, it is possible to find the immediately preceding nonprecipitating observation within a 24-h window. In contrast, when only using the GMI observations, only 37.26% of Δt are less than 24 h. The surface characteristics are much more likely to vary because of the larger Δt . Therefore, ΔTB more likely includes other information (e.g., new snow accumulation on the ground, snowpack melt, and refreezing) in addition to the current precipitation signal.

To show the variable Δt effect, the observations are divided into different categories based on Δt . Figure 11a shows that ΔTB from V89, V166, and V190 more weakly correlates with the precipitation rate as Δt increases. The ΔTB for other channels behaves similarly. As

mentioned previously, ΔTB is more likely to contain other signals besides the current precipitation signal with larger Δt . Similar analysis is performed over the Northeast region ($37^\circ\text{--}47^\circ\text{N}$, $65^\circ\text{--}80^\circ\text{W}$) and the Southeast region ($30^\circ\text{--}35^\circ\text{N}$, $80^\circ\text{--}90^\circ\text{W}$). Figure 11b shows that the correlation between precipitation rate, and ΔTB remains relatively unchanged with Δt less than 24 h. It is worth mentioning that by using eight sensors, the vast majority of Δt is less than 24 h (Fig. 10a). The magnitude of the correlation sharply decreases to 0 with Δt varying from 24 h (1 day) to 72 h (3 days). This implies that to effectively use the ΔTB signal, eight sensors are necessary over this region.

Over the Southeast region, the correlation is almost independent from the Δt variation. This feature implies that over this region observations from one satellite are sufficient to derive ΔTB . The physical reason is because the surface background is relatively homogeneous and less variable, compared with that over the Northeast region.

In a postprocessing mode, it is possible to find the closest nonprecipitating scene by checking the succeeding

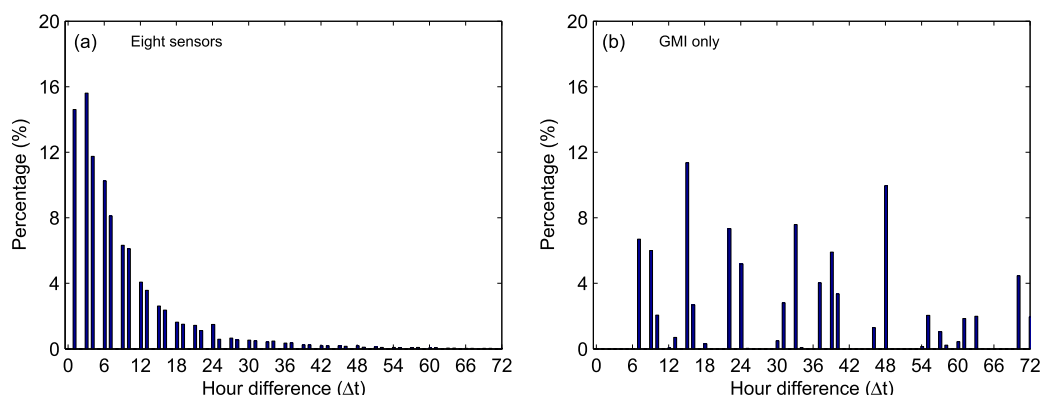


FIG. 10. (a) Histogram of the time difference [Δt in Eq. (3)] when using eight sensors, including GMI, ATMS, SSMIS (*F17*), SSMIS (*F18*), MHS (*NOAA-18*), MHS (*NOAA-19*), MHS(*MetOp-A*), and MHS (*MetOp-B*). (b) Histogram of the time difference [Δt in Eq. (3)] when using GMI only.

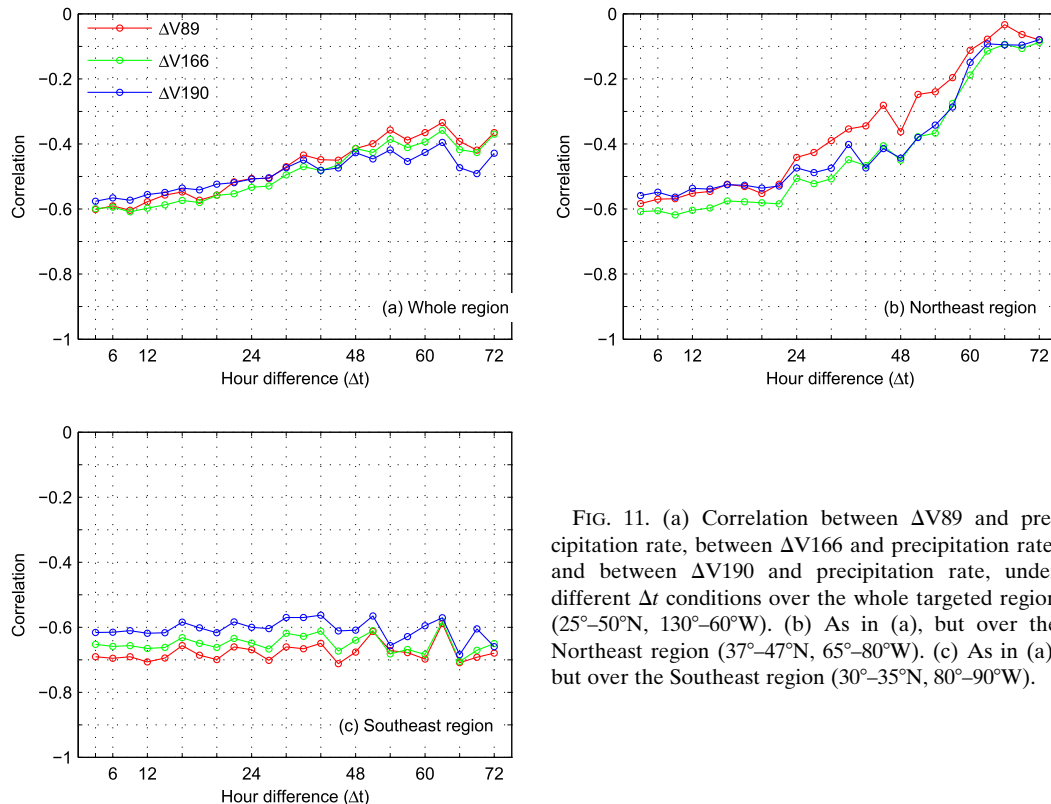


FIG. 11. (a) Correlation between $\Delta V89$ and precipitation rate, between $\Delta V166$ and precipitation rate, and between $\Delta V190$ and precipitation rate, under different Δt conditions over the whole targeted region (25° – 50° N, 130° – 60° W). (b) As in (a), but over the Northeast region (37° – 47° N, 65° – 80° W). (c) As in (a), but over the Southeast region (30° – 35° N, 80° – 90° W).

observations. By doing so, it can further shorten Δt , thereby obtaining a more accurate ΔTB . It is found that by choosing the nonprecipitating pixels with shorter time either from the preceding observations or from succeeding observations, the correlation between ΔTB and precipitation rate can be further improved. Specifically, about 80.35% (91.33%) of grid boxes have a stronger negative correlation when considering both preceding and succeeding observations for ΔTB computation, compared with only considering preceding (succeeding) observations.

To summarize, this section demonstrates that observations from these eight satellites significantly increase the revisit frequency, which is crucial for effectively exploiting the signature of ΔTB , especially over frequently snow-covered regions.

e. One sensor versus eight sensors

It is found in the previous section that Δt is much larger when only GMI observations are used. The much larger Δt can negatively affect the correlation between precipitation rate and ΔTB . This brings the question as to whether one should use ΔTB when a precipitation algorithm is developed for a single sensor. This section demonstrates the correlation between precipitation rate and TBs at each GMI channel, between precipitation rate and ΔTB of GMI based only on GMI observations,

and between precipitation rate and ΔTB of GMI based on observations from eight sensors. We choose GMI since it has the fewest observations (Table 2).

The first column of Fig. 12 shows the correlation between precipitation rate and GMI TB for its six channels. In the second column, we show the correlation between precipitation rate and ΔTB at the corresponding channel. The ΔTB here is computed using GMI-only observations. It is noted that even using GMI observations only, ΔTB significantly improves the correlation with precipitation rate, which is particularly evident in regions with cold surfaces (e.g., Rocky Mountains and north of 45° N) at 89 GHz (cf. Figs. 12a and 12b). Based on this result, it is recommended that ΔTB is preferred when retrieval algorithm is developed for a single sensor.

Next, we compute the correlation between precipitation rate and ΔTB , which is based on eight sensor observations. By using observations from these eight sensors, ΔTB performance is further improved. For example, the correlation between precipitation rate and $\Delta V89$ based on eight sensors is about -0.6 over most of the Rocky Mountain region and Northeast region (Fig. 12c). In contrast, the much smaller correlation at about -0.1 widely exists over the aforementioned two regions from $\Delta V89$ based on GMI only

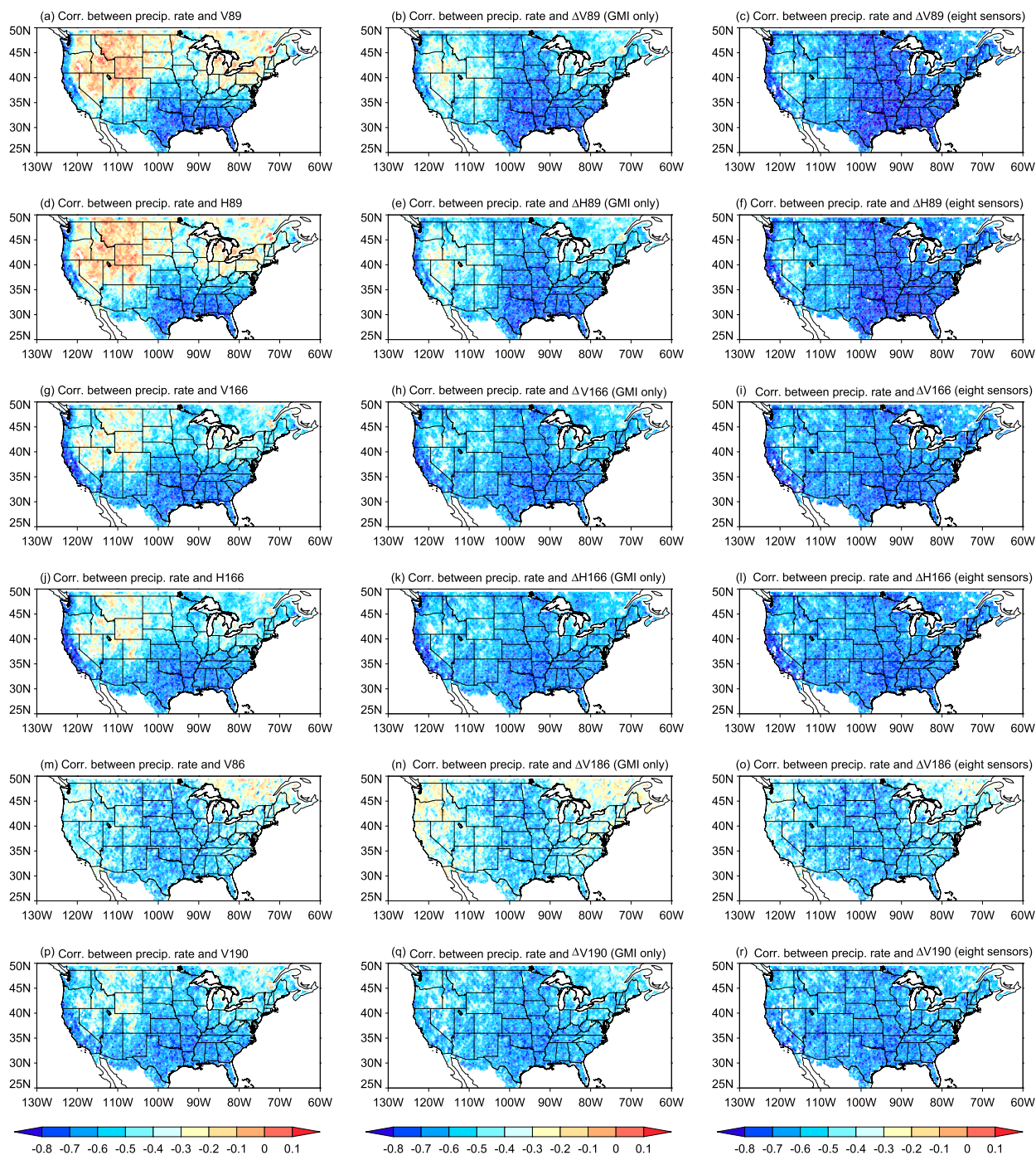


FIG. 12. (left) Correlation between the instantaneous TB and precipitation rate, using GMI observation only. (center) Correlation between precipitation rate and ΔTB at the corresponding channel, where ΔTB is derived from GMI observations only. (right) Correlation between precipitation rate and ΔTB at the corresponding channel, where ΔTB is derived from all eight sensor observations.

(Fig. 12b). A similar phenomenon is observed at other frequencies.

In summary, it is demonstrated that ΔTB based only on one sensor is more highly correlated with precipitation rate than the instantaneous TB, especially

over regions where snow accumulation is frequent in the winter season. In addition, we show that the correlation between ΔTB and precipitation rate is further improved when observations from eight sensors are utilized.

f. Retrieval performance

Previous sections have demonstrated that precipitation rate is more highly correlated with ΔTB than the instantaneous TB. In this section, we utilize a simple linear regression retrieval as a proof of concept to demonstrate the potential of ΔTB in a retrieval algorithm. Specifically, in each 25° grid box, a linear regression model is established, either between precipitation rate and TB or between precipitation rate and ΔTB . Data in 2014 and 2015 are used as the training dataset, and data in 2016 are taken as the validation. We would like to emphasize that more advanced statistical techniques (e.g., neural networks and Bayes' theorem) may further improve the retrieval performance. As a proof of concept, here we use the simple linear regression approach.

As mentioned previously, there are several sensors with the highest possible frequency at ~ 89 GHz (e.g., AMSU-A and AMSR-2). Therefore, we first apply this simple linear regression algorithm to V89 only, and then TBs at all frequencies are used to retrieve the precipitation rate.

1) RETRIEVAL RESULTS FROM V89 ONLY

Figure 13 shows the simple single-channel retrieval performance over the entire region and the Northeast (37° – 47° N, 65° – 80° W) and Southeast (30° – 35° N, 80° – 90° W) regions. The retrieval over the entire region based on $\Delta V89$ (Fig. 13b) clearly outperforms that from V89 itself (Fig. 13a). Specifically, the correlation, root-mean-square error (RMSE), and bias for the 2016 validation period from $\Delta V89$ are 0.64, 1.63 mm h^{-1} , and -7.20% , respectively. In contrast, they are 0.51, 1.83 mm h^{-1} , and -38.92% from V89 itself. The largest improvement is for the relative light precipitation with intensity less than 4 mm h^{-1} . It is pointed out earlier that the surface affects TB at 89 GHz to a larger extent under a light precipitation scenario.

Using V89 itself, the simple regression retrieval performance is very poor over the Northeast region with the correlation of 0.33, RMSE of 1.45 mm h^{-1} , and bias of -59.41% (Fig. 13c). However, these statistics are significantly improved from $\Delta V89$ (Fig. 13d). The correlation increases from 0.33 to 0.63, RMSE decreases from 1.45 to 1.18 mm h^{-1} , and the bias reduces from -59.41% to -13.98% .

In the Southeast region, the improvement is not as large as that over the Northeast region (cf. Figs. 13e and 13f). However, we indeed notice that there are large improvements in the lower end of the precipitation intensity distribution from 0.2 to 2 mm h^{-1} . In this range, the $\Delta V89$ clearly has smaller overestimation, which contributes to the smaller bias at -0.83% by ΔTB .

In summary, this section shows that the simple single-channel regression retrieval that results from $\Delta V89$ is much better than that from V89 itself. More importantly, over frequently snow-covered land regions, $\Delta V89$ performs very well. This opens new opportunities to use sensors with the highest possible frequency at ~ 89 GHz to retrieve precipitation at high latitudes (e.g., north of 45° N) in the winter season.

2) RETRIEVAL RESULTS FROM ALL CHANNELS

This section builds on the previous section and applies a multichannel regression retrieval to demonstrate the value of ΔTB . We first show a blizzard case over the Mid-Atlantic and northeastern United States on 23 January 2016. All eight sensors observed this event at different overpass times.

Figures 14 and 15 show the geospatial distribution of the retrieved precipitation rate from each of the eight sensors. Each row of Fig. 14 and Fig. 15 shows the MRMS observed precipitation, the retrieved precipitation from all TBs (V89, H89, ..., V190) for each sensor, and the retrieved precipitation from all ΔTB s ($\Delta V89$, $\Delta H89$, ..., $\Delta V190$) for each sensor. The overpass time for each sensor is shown in the title of each figure.

For GMI, it is noted that the retrieval results from ΔTB (Fig. 14c) are able to better capture the heaviest precipitation center located around the boundary among West Virginia, Maryland, and Pennsylvania. More importantly, the overestimation based on TB (Fig. 14b) is obvious from northern Pennsylvania to New York. This overestimation is primarily caused by cold land surface contamination, which is largely alleviated by ΔTB .

For ATMS (second row of Fig. 14), retrieval results from both TB (Fig. 14e) and ΔTB (Fig. 14f) capture the heavy snowfall center. However, the overestimation around the heavy snowfall center based on TB is evident (cf. Fig. 14d and Fig. 14e). This overestimation is largely eliminated from the ΔTB result. Similar features are observed for MHS (NOAA-I8; third row of Fig. 14), MHS (NOAA-I9; fourth row of Fig. 14), SSMIS (F17; third row of Fig. 15), and SSMIS (F18; fourth row of Fig. 15). For MHS (MetOp-A; first row of Fig. 15) and MHS (MetOp-B; second row of Fig. 15), both TB and ΔTB severely underestimated the precipitation rate (cf. Figs. 15a and 15b).

The value of the ΔTB -based retrieval is further demonstrated through the scatterplots in Fig. 16. The most striking feature in the scatterplots is that the overestimation with reference MRMS precipitation rates less than 2 mm h^{-1} is greatly alleviated for all sensors (cf. Figs. 16a and 16b). Improvement for heavier precipitation rates ($>2 \text{ mm h}^{-1}$) is also clearly

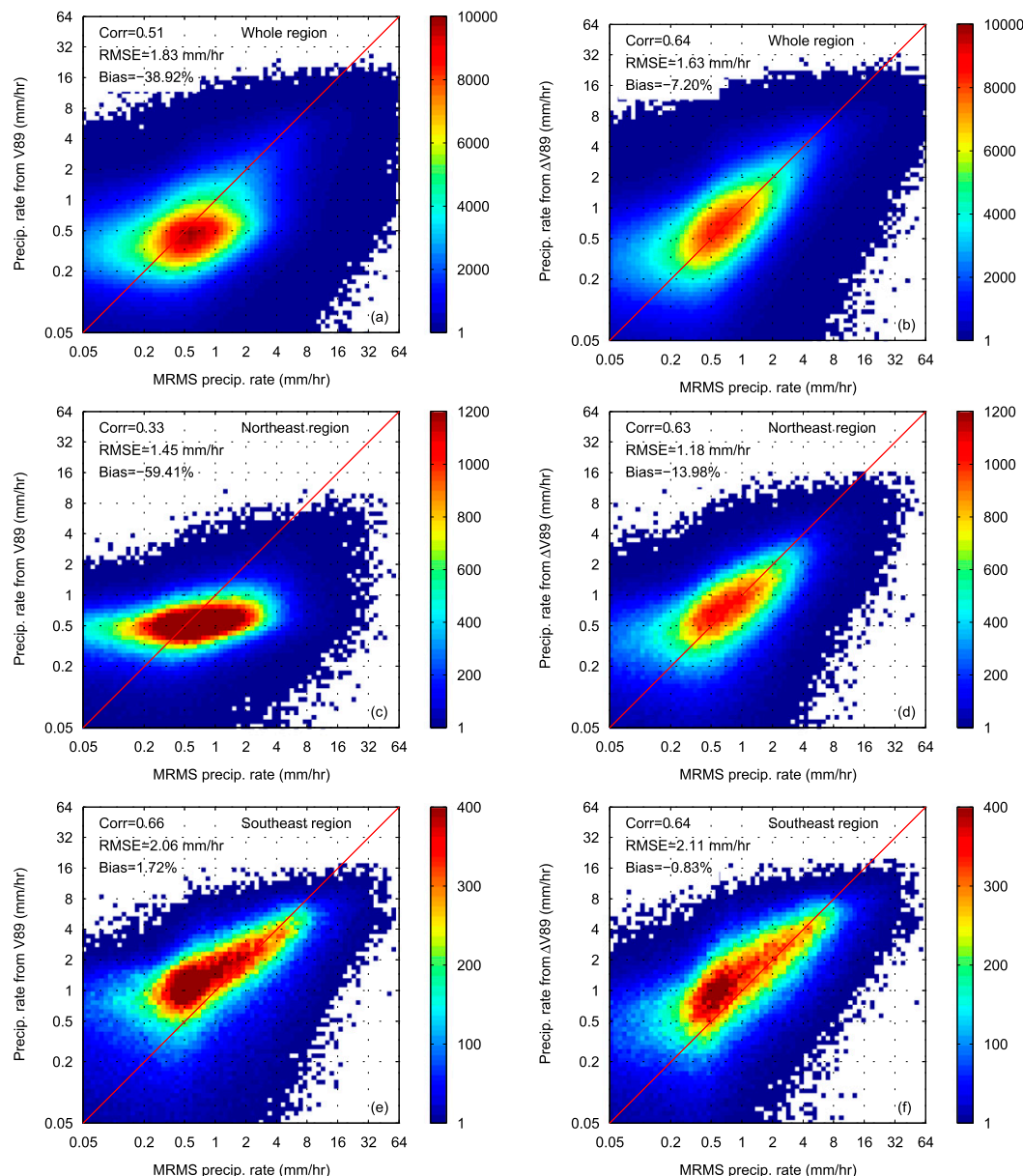


FIG. 13. Precipitation retrieval performance in 2016 by using V89 and $\Delta V89$. (a) Density scatterplot between MRMS (reference) and retrieved precipitation rate from V89 over the whole area. (b) Scatterplot between MRMS (reference) and retrieved precipitation rate from $\Delta V89$ over the whole area. (c) As in (a), but over the Northeast region (37° – 47° N, 65° – 80° W). (d) As in (b), but over the Northeast region (37° – 47° N, 65° – 80° W). (e) As in (a), but over the Southeast region (30° – 35° N, 80° – 90° W). (f) As in (b), but over the Southeast region (30° – 35° N, 80° – 90° W).

noticeable for GMI (cf. Figs. 16a and 16b), MHS (*NOAA-18*; cf. Figs. 16e and 16f), SSMIS (*F17*; cf. Figs. 16m and 16n), and SSMIS (*F18*; cf. Figs. 16o and 16p).

The correlation, RMSE, and bias for each sensor from this event are listed in Table 3. Better statistics from ΔTB are observed for all sensors with bias for MHS (*MetOp-A*) as an exception, which is explained below. Specifically, for GMI, the correlation increases from

0.27 based on TB to 0.76 based on ΔTB , RMSE reduces from 1.34 to 0.72 mm h^{-1} , and the bias reduces from 40.04% to 8.03%. Similar degrees of improvements are obtained from SSMIS (*F17*) and SSMIS (*F18*). For ATMS, the bias is greatly improved from 30.36% based on TB to -4.36% based on ΔTB .

Marked improvement also has been found for multi-channel regression retrieval performance based on ΔTB from MHS (*NOAA-18*), MHS (*NOAA-19*), and

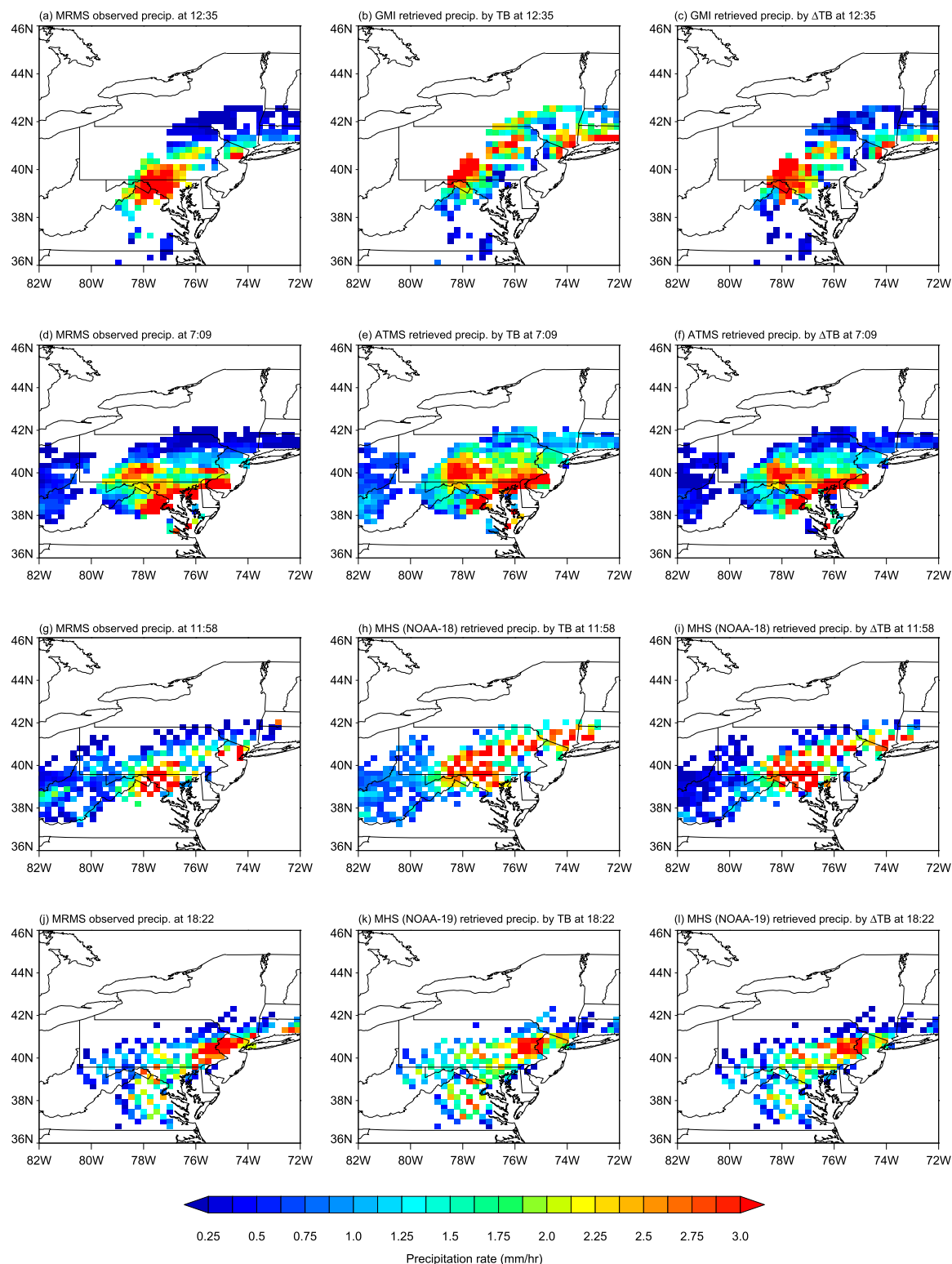


FIG. 14. Case study of the blizzard case over the U.S. Mid-Atlantic and Northeast on 23 Jan 2016. Each row shows the MRMS observed precipitation, the retrieved precipitation from TBs themselves for each sensor, and the retrieved precipitation from Δ TBs for each sensor. The overpass time for each sensor is shown in the title of each figure. (a)–(c) GMI, (d)–(f) ATMS, (g)–(i) MHS (NOAA-18), and (j)–(l) MHS (NOAA-19).

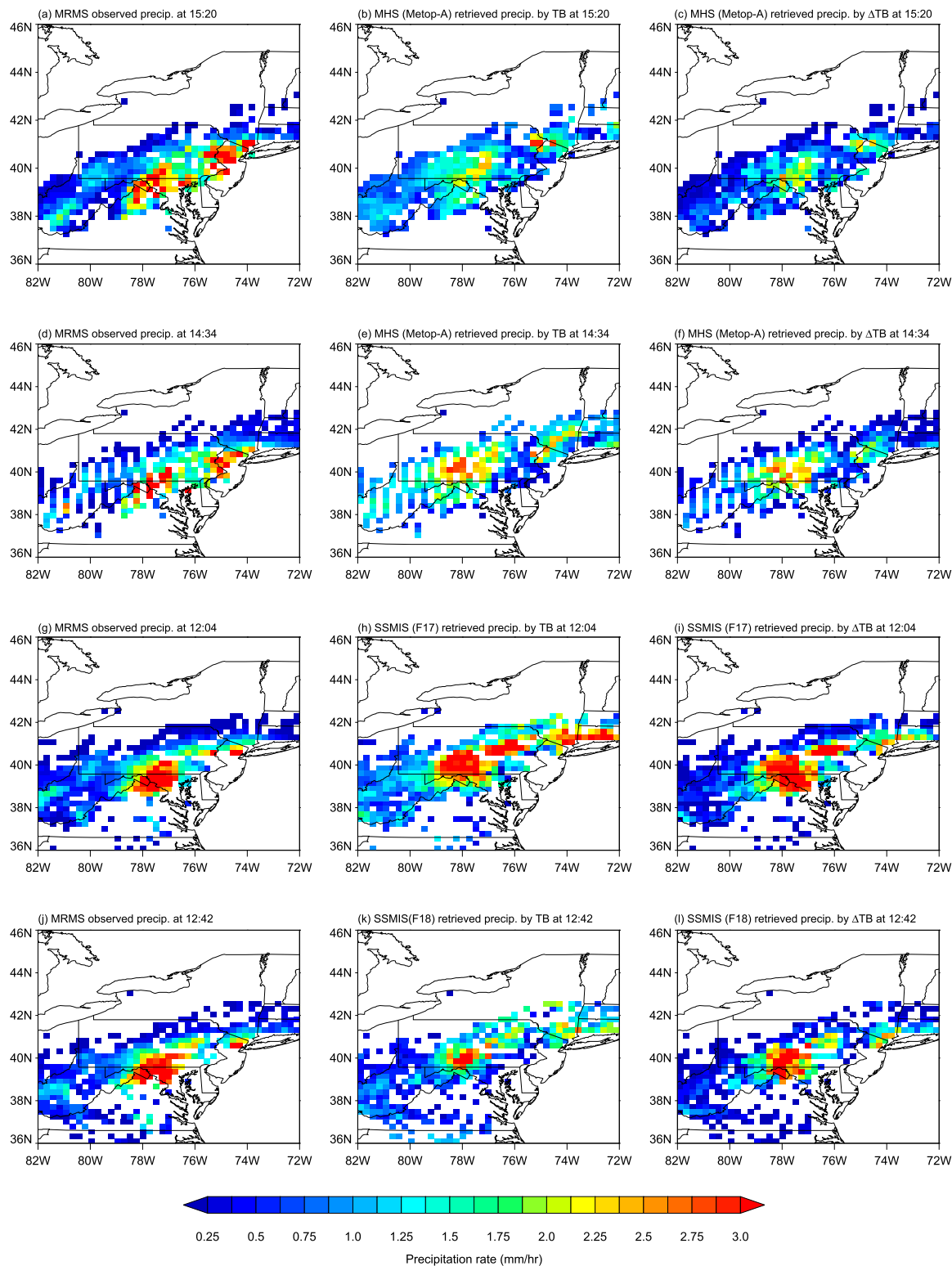


FIG. 15. As in Fig. 14, but for sensors of MHS (*MetOp-A*), MHS (*MetOp-B*), SSMIS (*F17*), and SSMIS (*F18*), respectively.

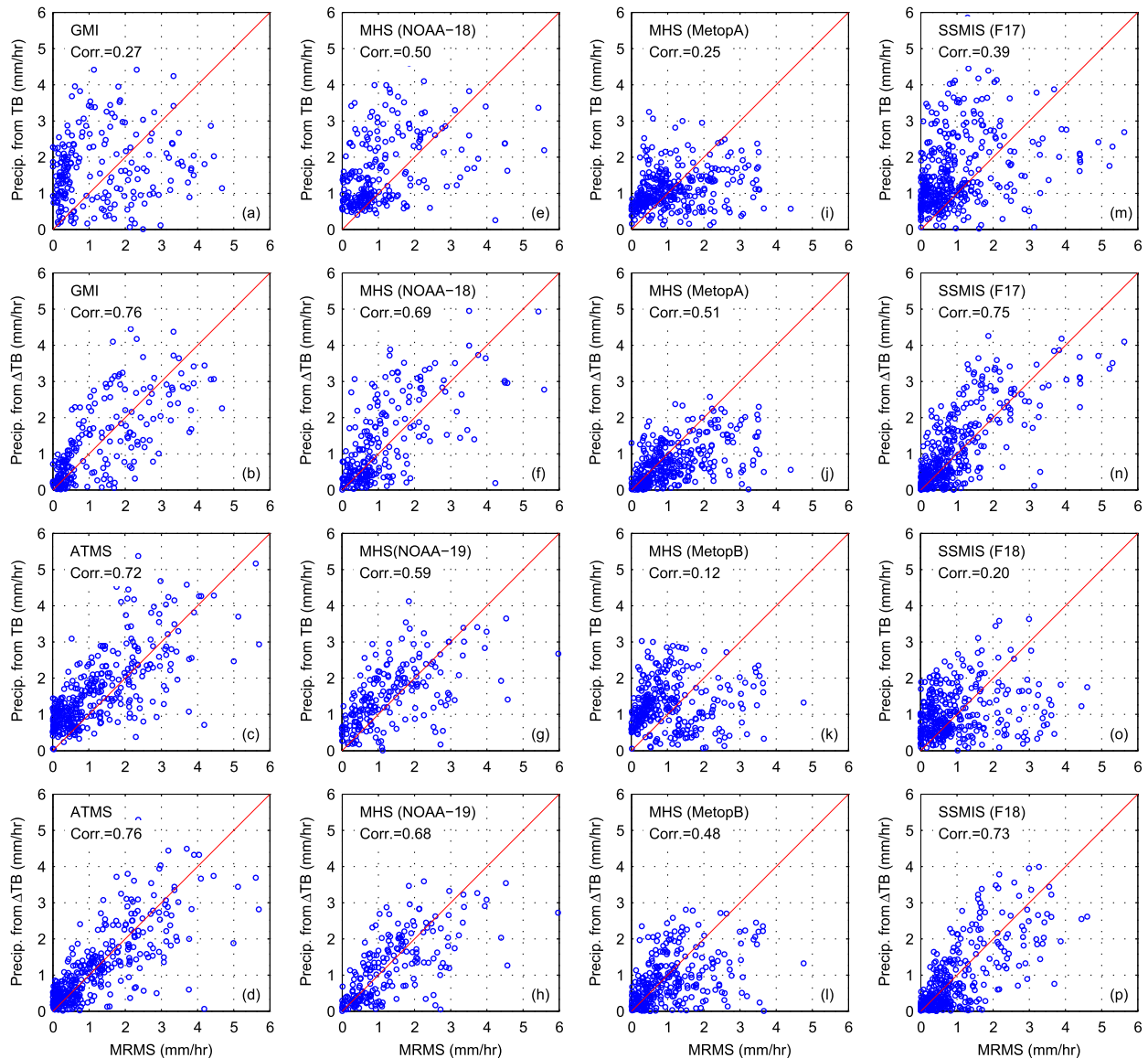


FIG. 16. Scatterplots between MRMS precipitation rate and retrieved precipitation rate from all eight sensors based on all TBs, and between MRMS precipitation rate and retrieved precipitation rate from all eight sensors based on all Δ TBs (Δ V89, ..., Δ V190), for the blizzard event over the Mid-Atlantic and Northeast on 23 Jan 2016. Only the correlation coefficient is labeled in the figure because of space limitations. RMSE and bias are listed in Table 3.

MHS (*MetOp-B*). As mentioned previously, the magnitude of the bias based on Δ TB from MHS (*MetOp-A*) is larger than that based on TB, although the correlation and RMSE is improved by Δ TB. The reason is that the overestimation for precipitation rates less than 2 mm h^{-1} is mitigated (cf. Figs. 16i and 16j). However, the underestimation with precipitation rates larger than 2 mm h^{-1} is not improved. Therefore, it ends up with a larger negative bias (-40.09%).

Next, the retrieval performance is assessed over the whole region and the Northeast and Southeast regions.

Figures 17a and 17b show the overall retrieval results from TBs and Δ TBs in the targeted region. It is clear that the performance from Δ TBs is superior, as indicated by better statistics. Specifically, the correlation, RMSE, and bias based on the instantaneous TB (Fig. 17a) are 0.58, 1.75 mm h^{-1} , and -13.50% , respectively. Using Δ TB, these statistics are improved to 0.65, 1.64 mm h^{-1} , and -3.86% (Fig. 17b). Similar to the V89 only retrieval result over the Northeast region, much larger improvements have been noticed (cf. Figs. 17c and 17d). In this region, by using Δ TB the correlation improved from 0.44

TABLE 3. Correlation, RMSE, and bias based on TB and Δ TB from each of the eight sensors, for the blizzard case over the Mid-Atlantic and Northeast regions of the United States on 23 Jan 2016.

	Correlation		RMSE (mm h ⁻¹)		Bias (%)	
	TB	Δ TB	TB	Δ TB	TB	Δ TB
GMI (GPM)	0.27	0.76	1.34	0.72	40.03	8.03
ATMS (<i>SNPP</i>)	0.72	0.76	0.83	0.69	30.36	-4.36
MHS (<i>NOAA-18</i>)	0.50	0.69	0.99	0.75	39.98	14.36
MHS (<i>NOAA-19</i>)	0.59	0.68	0.89	0.79	12.48	-9.90
MHS (<i>MetOp-A</i>)	0.25	0.51	0.94	0.83	11.00	-40.09
MHS (<i>MetOp-B</i>)	0.12	0.48	1.06	0.82	24.21	-18.04
SSMIS (<i>F17</i>)	0.39	0.75	1.11	0.61	49.72	16.40
SSMIS (<i>F18</i>)	0.20	0.73	0.94	0.57	38.79	0.85

to 0.61, RMSE reduced from 1.35 to 1.22 mm h⁻¹, and the bias decreased from -14.18% to -8.38%. While in the U.S. Southeast, improvement is more noticeable for precipitation intensities less than 2 mm h⁻¹ (cf. Figs. 17e and 17f).

Seasonal retrieval performance is also evaluated. Figures are not shown because of space limitations. Retrieval results from Δ TBs are better over all the regions in all four seasons, as indicated by the better statistics. The improvement for the intensity from 0 to 2 mm h⁻¹ over the Southeast region is especially obvious in the winter season, because the precipitation signal is weaker in winter (compared with that in summer), and any contamination due to the environmental variation will negatively impact the results to a larger degree.

5. Conclusions and discussions

This study proposes a new approach to improve precipitation rate retrievals over land: using TB temporal variation Δ TB. We test this idea by using observations from eight sensors on board polar-orbiting satellites in the current GPM microwave radiometer constellation, including GMI, SSMIS (*F17*), SSMIS (*F18*), ATMS, MHS (*NOAA-18*), MHS (*NOAA-19*), MHS (*MetOp-A*), and MHS (*MetOp-B*). MRMS precipitation rate over the land portion of 25°–50°N, 130°–60°W from March 2014 to December 2016 is the reference data for this study. In this study, only the high-frequency channels from 89 to 183.3 GHz are used since they are commonly available in all aforementioned eight sensors.

We first developed a method to convert TBs from other sensors to GMI channels. Time series analysis shows no obvious bias from this conversion. By doing so, the observation frequency is significantly increased. Specifically, the revisit frequency for any single sensor in the targeted region is less than 2 times daily. By combining all the observations from these eight sensors, the

revisit frequency is increased to 10–16 times daily, depending on the latitude. Further analysis shows that the much more frequent revisits for a certain location are crucial to obtain stronger correlation between Δ TB and precipitation rate.

We demonstrate that Δ TB correlates more strongly with precipitation rate than the instantaneous TB for all channels. The largest improvement in correlation is in the winter season. The primary reason is that misidentified pixels with snow accumulation on the ground have much less influence on Δ TB, while these pixels can significantly alter the relation between the instantaneous TB and precipitation rate. The Δ TB also is relatively insensitive to the environmental variation (e.g., temperature and humidity variations from summer to winter), while TBs (especially TB at 89 GHz) are affected by environmental variation. This is the reason why even in the southeastern United States, Δ TB outperforms the instantaneous TB.

Further analysis shows that the correlation between Δ TB and precipitation rate is highly dependent on the time difference Δt . The Δ TB is correlated more strongly with precipitation rate as Δt decreases. The longer the Δt , the more likely Δ TBs include other information (new snow accumulation on the ground, snowmelt and refreezing, etc.) besides the current precipitation signature.

A simple single-channel regression precipitation retrieval proof of concept shows that by only using Δ V89 the retrieved precipitation results agree very well with the reference MRMS precipitation rate. On the other hand, V89 itself performs much worse. This result opens a new opportunity for the sensors with the highest frequency at ~89 GHz to retrieve precipitation in snow-covered regions, which is currently avoided in practice by algorithms that use the instantaneous TB.

Analysis from a 2016 blizzard case over the United States demonstrates that the major limitation of using TB directly is the overestimation at the low intensity end of the precipitation rate distribution, where surface contamination plays a larger role. Finally, it is shown that a multichannel regression retrieval based on all Δ TBs (Δ V89, Δ H89, ..., Δ V190) is superior to that based on all TBs (V89, H89, ..., V190), as indicated by better statistics against the MRMS reference data. The improvement is particularly evident over frequently snow-covered regions.

One key step of this study is to identify the precipitation status for each observation, which directly affects the Δ TB computation. This study only uses the TBs for precipitation screening. Previous work (You et al. 2015) showed that detection performance can be

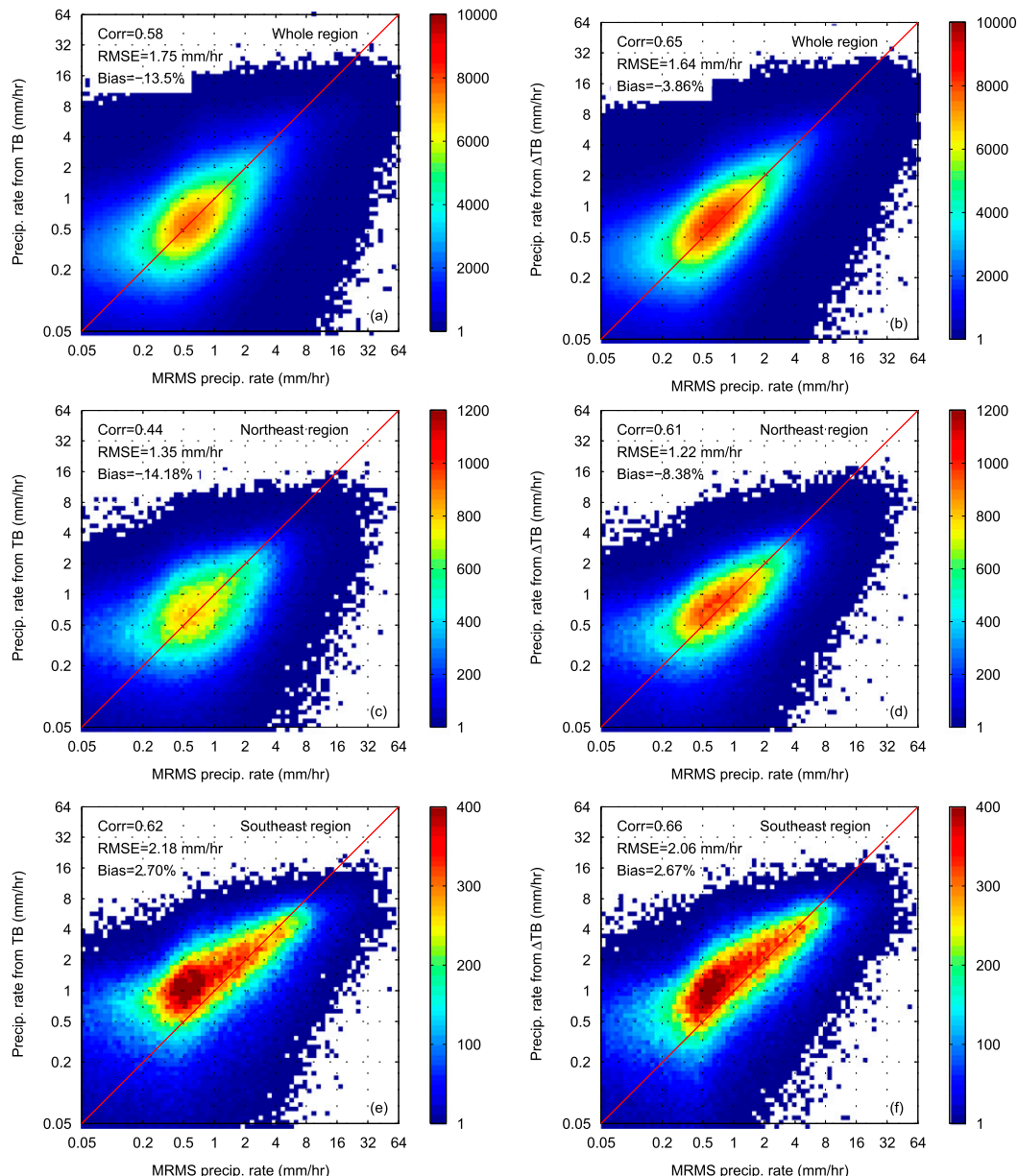


FIG. 17. Precipitation retrieval performance in 2016 by using all TBs (V89, . . . , V190) and all Δ TBs (Δ V89, . . . , Δ V190). (a) Density scatterplot between MRMS (reference) and retrieved precipitation rate from all TBs over the whole area. (b) Scatterplot between MRMS (reference) and retrieved precipitation rate from Δ TBs over the whole area. (c) As in (a), but over the Northeast region (37° – 47° N, 65° – 80° W). (d) As in (b), but over the Northeast region (37° – 47° N, 65° – 80° W). (e) As in (a), but over the Southeast region (30° – 35° N, 80° – 90° W). (f) As in (b), but over the Southeast region (30° – 35° N, 80° – 90° W).

further improved by including ancillary information, for example, land surface classification, lower tropospheric relative humidity and vertical velocity from reanalysis data, which is left for future work.

Not only does this study highlight the importance of maintaining the current microwave constellation, it also implies that a geostationary microwave radiometer can

significantly improve the precipitation retrieval over frequently snow-covered regions, by capitalizing on the surface and atmosphere “background” information contained in TB temporal variation.

Future work seeks to 1) extend this work to the GPM-covered land regions (65° S– 65° N), through incorporation of Δ TB in the Goddard profiling algorithm (GPROF),

where the GPM dual-frequency precipitation radar observations can be taken as the reference, and 2) extend this work to the ocean surface. Over the ocean surface, it is planned to compute TB temporal variation for both the high-frequency and low-frequency channels.

Acknowledgments. All satellite data are downloaded from NASA Precipitation Processing System (PPS) website (<https://storm.pps.eosdis.nasa.gov/storm/>). MRMS precipitation data are downloaded from the National Centers for Environmental Prediction (NCEP; <http://mrms.ncep.noaa.gov/data/>). We thank Dr. Wesley Berg for the information on SSMIS status. Comments by Dr. Joseph Munchak were very helpful in improving the original manuscript. The Equatorial Crossing Time (ECT) is provided by Dr. Eric Nelkin. This work is supported by NASA's Precipitation Measurement Missions Program science team via solicitation NNH15ZDA001N-PMM. Dr. Song Yang also would like to acknowledge the financial support from NRL base project "River Influence at Multi-scales (PE 61153N)." The authors would like to acknowledge the support from colleagues in the PMM Land Surface Working Group (LSWG).

REFERENCES

- Aonashi, K., and Coauthors, 2009: GSMaP passive microwave precipitation retrieval algorithm: Algorithm description and validation. *J. Meteor. Soc. Japan*, **87A**, 119–136, doi:[10.2151/jmsj.87A.119](https://doi.org/10.2151/jmsj.87A.119).
- Behrangi, A., H. Nguyen, B. Lambriksen, M. Schreier, and V. Dang, 2015: Investigating the role of multi-spectral and near surface temperature and humidity data to improve precipitation detection at high latitudes. *Atmos. Res.*, **163**, 2–12, doi:[10.1016/j.atmosres.2014.10.019](https://doi.org/10.1016/j.atmosres.2014.10.019).
- Berg, W., and Coauthors, 2016: Intercalibration of the GPM microwave radiometer constellation. *J. Atmos. Oceanic Technol.*, **33**, 2639–2654, doi:[10.1175/JTECH-D-16-0100.1](https://doi.org/10.1175/JTECH-D-16-0100.1).
- Boukabara, S.-A., and Coauthors, 2011: MiRS: An all-weather 1DVAR satellite data assimilation and retrieval system. *IEEE Trans. Geosci. Remote Sens.*, **49**, 3249–3272, doi:[10.1109/TGRS.2011.2158438](https://doi.org/10.1109/TGRS.2011.2158438).
- , and Coauthors, 2013: A physical approach for a simultaneous retrieval of sounding, surface, hydrometeor, and cryospheric parameters from SNPP/ATMS. *J. Geophys. Res. Atmos.*, **118**, 12 600–12 619, doi:[10.1002/2013JD020448](https://doi.org/10.1002/2013JD020448).
- Chen, F. W., and D. H. Staelin, 2003: AIRS/AMSU/HSB precipitation estimates. *IEEE Trans. Geosci. Remote Sens.*, **41**, 410–417, doi:[10.1109/TGRS.2002.808322](https://doi.org/10.1109/TGRS.2002.808322).
- Chen, S., and Coauthors, 2013: Evaluation and uncertainty estimation of NOAA/NSSL next-generation national mosaic quantitative precipitation estimation product (Q2) over the continental United States. *J. Hydrometeor.*, **14**, 1308–1322, doi:[10.1175/JHM-D-12-0150.1](https://doi.org/10.1175/JHM-D-12-0150.1).
- , and Coauthors, 2016: Comparison of snowfall estimates from the NASA CloudSat Cloud Profiling Radar and NOAA/NSSL Multi-Radar Multi-Sensor system. *J. Hydrol.*, **541**, 862–872, doi:[10.1016/j.jhydrol.2016.07.047](https://doi.org/10.1016/j.jhydrol.2016.07.047).
- Draper, D. W., D. Newell, F. J. Wentz, S. Krimchansky, and G. M. Skofronick-Jackson, 2015: The Global Precipitation Measurement (GPM) Microwave Imager (GMI): Instrument overview and early on-orbit performance. *IEEE J. Sel. Top. Appl. Earth Obs. Remote Sens.*, **8**, 3452–3462, doi:[10.1109/JSTARS.2015.2403303](https://doi.org/10.1109/JSTARS.2015.2403303).
- Ebtehaj, A. M., R. L. Bras, and E. Foufoula-Georgiou, 2015: Shrunk locally linear embedding for passive microwave retrieval of precipitation. *IEEE Trans. Geosci. Remote Sens.*, **53**, 3720–3736, doi:[10.1109/TGRS.2014.2382436](https://doi.org/10.1109/TGRS.2014.2382436).
- Ferraro, R. R., and G. F. Marks, 1995: The development of SSM/I rain-rate retrieval algorithms using ground-based radar measurements. *J. Atmos. Oceanic Technol.*, **12**, 755–770, doi:[10.1175/1520-0426\(1995\)012<0755:TDOSRR>2.0.CO;2](https://doi.org/10.1175/1520-0426(1995)012<0755:TDOSRR>2.0.CO;2).
- , E. A. Smith, W. Berg, and G. J. Huffman, 1998: A screening methodology for passive microwave precipitation retrieval algorithms. *J. Atmos. Sci.*, **55**, 1583–1600, doi:[10.1175/1520-0469\(1998\)055<1583:ASMFPM>2.0.CO;2](https://doi.org/10.1175/1520-0469(1998)055<1583:ASMFPM>2.0.CO;2).
- , and Coauthors, 2005: NOAA operational hydrological products derived from the advanced microwave sounding unit. *IEEE Trans. Geosci. Remote Sens.*, **43**, 1036–1049, doi:[10.1109/TGRS.2004.843249](https://doi.org/10.1109/TGRS.2004.843249).
- Gaier, T., and Coauthors, 2016: A 180 GHz prototype for a geostationary microwave imager/sounder-GeoSTAR-III. *IEEE Int. Geoscience and Remote Sensing Symp.*, Beijing, China, IEEE, 2021–2023, doi:[10.1109/IGARSS.2016.7729521](https://doi.org/10.1109/IGARSS.2016.7729521).
- Gopalan, K., N.-Y. Wang, R. Ferraro, and C. Liu, 2010: Status of the TRMM 2A12 land precipitation algorithm. *J. Atmos. Oceanic Technol.*, **27**, 1343–1354, doi:[10.1175/2010JTECHA1454.1](https://doi.org/10.1175/2010JTECHA1454.1).
- Grody, N., J. Zhao, R. Ferraro, F. Weng, and R. Boers, 2001: Determination of precipitable water and cloud liquid water over oceans from the NOAA 15 advanced microwave sounding unit. *J. Geophys. Res.*, **106**, 2943–2953, doi:[10.1029/2000JD900616](https://doi.org/10.1029/2000JD900616).
- Helfrich, S. R., D. McNamara, B. H. Ramsay, T. Baldwin, and T. Kasheta, 2007: Enhancements to, and forthcoming developments in the Interactive Multisensor Snow and Ice Mapping System (IMS). *Hydrol. Processes*, **21**, 1576–1586, doi:[10.1002/hyp.6720](https://doi.org/10.1002/hyp.6720).
- Islam, T., P. K. Srivastava, Q. Dai, M. Gupta, and L. Zhuo, 2015: Rain rate retrieval algorithm for conical-scanning microwave imagers aided by random forest, RReliefF, and multivariate adaptive regression splines (RAMARS). *IEEE Sens. J.*, **15**, 2186–2193, doi:[10.1109/JSEN.2014.2372814](https://doi.org/10.1109/JSEN.2014.2372814).
- Kidd, C., T. Matsui, J. Chern, K. Mohr, C. Kummerow, and D. Randel, 2016: Global precipitation estimates from cross-track passive microwave observations using a physically based retrieval scheme. *J. Hydrometeor.*, **17**, 383–400, doi:[10.1175/JHM-D-15-0051.1](https://doi.org/10.1175/JHM-D-15-0051.1).
- Kummerow, C. D., and Coauthors, 2001: The evolution of the Goddard Profiling Algorithm (GPROF) for rainfall estimation from passive microwave sensors. *J. Appl. Meteor.*, **40**, 1801–1820, doi:[10.1175/1520-0450\(2001\)040<1801:TEOTGP>2.0.CO;2](https://doi.org/10.1175/1520-0450(2001)040<1801:TEOTGP>2.0.CO;2).
- , S. Ringerud, J. Crook, D. Randel, and W. Berg, 2011: An observationally generated a priori database for microwave rainfall retrievals. *J. Atmos. Oceanic Technol.*, **28**, 113–130, doi:[10.1175/2010JTECHA1468.1](https://doi.org/10.1175/2010JTECHA1468.1).
- , D. L. Randel, M. Kulie, N.-Y. Wang, R. Ferraro, S. Joseph Munchak, and V. Petkovic, 2015: The evolution of the Goddard Profiling Algorithm to a fully parametric scheme.

- J. Atmos. Oceanic Technol.*, **32**, 2265–2280, doi:[10.1175/JTECH-D-15-0039.1](https://doi.org/10.1175/JTECH-D-15-0039.1).
- Lambrigtsen, B., A. Tanner, T. Gaier, P. Kangaslahti, and S. Brown, 2006: A microwave sounder for GOES-R: Developing the GeoSTAR mission. *IEEE Int. Geoscience and Remote Sensing Symp.*, Denver, CO, IEEE, 3964–3967, doi:[10.1109/IGARSS.2006.1017](https://doi.org/10.1109/IGARSS.2006.1017).
- Laviola, S., and V. Levizzani, 2011: The 183-WSL fast rain rate retrieval algorithm: Part I: Retrieval design. *Atmos. Res.*, **99**, 443–461, doi:[10.1016/j.atmosres.2010.11.013](https://doi.org/10.1016/j.atmosres.2010.11.013).
- Liu, G., and J. A. Curry, 1992: Retrieval of precipitation from satellite microwave measurement using both emission and scattering. *J. Geophys. Res.*, **97**, 9959–9974, doi:[10.1029/92JD00289](https://doi.org/10.1029/92JD00289).
- McCollum, J. R., and R. R. Ferraro, 2003: Next generation of NOAA/NESDIS TMI, SSM/I, and AMSR-E microwave land rainfall algorithms. *J. Geophys. Res.*, **108**, 8382, doi:[10.1029/2001JD001512](https://doi.org/10.1029/2001JD001512).
- Meyers, P. C., and R. R. Ferraro, 2016: Precipitation from the Advanced Microwave Scanning Radiometer 2. *IEEE J. Sel. Top. Appl. Earth Obs. Remote Sens.*, **9**, 2611–2618, doi:[10.1109/JSTARS.2015.2513666](https://doi.org/10.1109/JSTARS.2015.2513666).
- Noh, Y.-J., G. Liu, E.-K. Seo, J. R. Wang, and K. Aonashi, 2006: Development of a snowfall retrieval algorithm at high microwave frequencies. *J. Geophys. Res.*, **111**, D22216, doi:[10.1029/2005JD006826](https://doi.org/10.1029/2005JD006826).
- Petty, G. W., 1994: Physical retrievals of over-ocean rain rate from multichannel microwave imagery. Part II: Algorithm implementation. *Meteor. Atmos. Phys.*, **54**, 101–121, doi:[10.1007/BF01030054](https://doi.org/10.1007/BF01030054).
- , and K. Li, 2013: Improved passive microwave retrievals of rain rate over land and ocean. Part II: Validation and intercomparison. *J. Atmos. Oceanic Technol.*, **30**, 2509–2526, doi:[10.1175/JTECH-D-12-00184.1](https://doi.org/10.1175/JTECH-D-12-00184.1).
- Sanò, P., D. Casella, A. Mugnai, G. Schiavon, E. A. Smith, and G. J. Tripoli, 2013: Transitioning from CRD to CDRD in Bayesian retrieval of rainfall from satellite passive microwave measurements: Part 1. Algorithm description and testing. *IEEE Trans. Geosci. Remote Sens.*, **51**, 4119–4143, doi:[10.1109/TGRS.2012.2227332](https://doi.org/10.1109/TGRS.2012.2227332).
- , G. Panegrossi, D. Casella, F. Di Paola, L. Milani, A. Mugnai, M. Petracca, and S. Dietrich, 2015: The Passive Microwave Neural Network Precipitation Retrieval (PNPR) algorithm for AMSU/MHS observations: Description and application to European case studies. *Atmos. Meas. Tech.*, **8**, 837–857, doi:[10.5194/amt-8-837-2015](https://doi.org/10.5194/amt-8-837-2015).
- Shige, S., and Coauthors, 2009: The GSMap precipitation retrieval algorithm for microwave sounders—Part I: Over-ocean algorithm. *IEEE Trans. Geosci. Remote Sens.*, **47**, 3084–3097, doi:[10.1109/TGRS.2009.2019954](https://doi.org/10.1109/TGRS.2009.2019954).
- Spencer, R. W., H. M. Goodman, and R. E. Hood, 1989: Precipitation retrieval over land and ocean with the SSM/I: Identification and characteristics of the scattering signal. *J. Atmos. Oceanic Technol.*, **6**, 254–273, doi:[10.1175/1520-0426\(1989\)006<0254:PROLAO>2.0.CO;2](https://doi.org/10.1175/1520-0426(1989)006<0254:PROLAO>2.0.CO;2).
- Staelin, D. H., and F. W. Chen, 2000: Precipitation observations near 54 and 183 GHz using the noaa-15 satellite. *IEEE Trans. Geosci. Remote Sens.*, **38**, 2322–2332, doi:[10.1109/36.868889](https://doi.org/10.1109/36.868889).
- Surussavadee, C., and D. H. Staelin, 2008: Global millimeter-wave precipitation retrievals trained with a cloud-resolving numerical weather prediction model, Part I: Retrieval design. *IEEE Trans. Geosci. Remote Sens.*, **46**, 99–108, doi:[10.1109/TGRS.2007.908302](https://doi.org/10.1109/TGRS.2007.908302).
- , and —, 2010: Npoess precipitation retrievals using the ATMS passive microwave spectrometer. *IEEE Geosci. Remote Sens. Lett.*, **7**, 440–444, doi:[10.1109/LGRS.2009.2038614](https://doi.org/10.1109/LGRS.2009.2038614).
- Tang, L., Y. Tian, and X. Lin, 2014: Validation of precipitation retrievals over land from satellite-based passive microwave sensors. *J. Geophys. Res. Atmos.*, **119**, 4546–4567, doi:[10.1002/2013JD020933](https://doi.org/10.1002/2013JD020933).
- Tian, Y., C. D. Peters-Lidard, K. W. Harrison, Y. You, S. Ringerud, S. Kumar, and F. J. Turk, 2015: An examination of methods for estimating land surface microwave emissivity. *J. Geophys. Res. Atmos.*, **120**, 11 114–11 128, doi:[10.1002/2015JD023582](https://doi.org/10.1002/2015JD023582).
- Turk, F. J., Z. S. Haddad, and Y. You, 2014: Principal components of multifrequency microwave land surface emissivities. Part I: Estimation under clear and precipitating conditions. *J. Hydrometeorol.*, **15**, 3–19, doi:[10.1175/JHM-D-13-08.1](https://doi.org/10.1175/JHM-D-13-08.1).
- , —, and —, 2016: Estimating nonraining surface parameters to assist GPM constellation radiometer precipitation algorithms. *J. Atmos. Oceanic Technol.*, **33**, 1333–1353, doi:[10.1175/JTECH-D-15-0229.1](https://doi.org/10.1175/JTECH-D-15-0229.1).
- Viltard, N., C. Burlaud, and C. D. Kummerow, 2006: Rain retrieval from TMI brightness temperature measurements using a TRMM PR-based database. *J. Appl. Meteor. Climatol.*, **45**, 455–466, doi:[10.1175/JAM2346.1](https://doi.org/10.1175/JAM2346.1).
- Wang, N.-Y., C. Liu, R. Ferraro, D. Wolff, E. Zipser, and C. Kummerow, 2009: TRMM 2A12 land precipitation product-status and future plans. *J. Meteor. Soc. Japan*, **87A**, 237–253, doi:[10.2151/jmsj.87A.237](https://doi.org/10.2151/jmsj.87A.237).
- Weng, F., L. Zhao, R. R. Ferraro, G. Poe, X. Li, and N. C. Grody, 2003: Advanced microwave sounding unit cloud and precipitation algorithms. *Radio Sci.*, **38**, 8068, doi:[10.1029/2002RS002679](https://doi.org/10.1029/2002RS002679).
- Wilks, D. S., 2011: *Statistical Methods in the Atmospheric Sciences*. 3rd ed. International Geophysics Series, Vol. 100, Academic Press, 704 pp.
- Yang, S., F. Weng, B. Yan, N. Sun, and M. Goldberg, 2011: Special Sensor Microwave Imager (SSM/I) intersensor calibration using a simultaneous conical overpass technique. *J. Appl. Meteor. Climatol.*, **50**, 77–95, doi:[10.1175/2010JAMC2271.1](https://doi.org/10.1175/2010JAMC2271.1).
- , J. Hawkins, and K. Richardson, 2014: The improved NRL tropical cyclone monitoring system with a unified microwave brightness temperature calibration scheme. *Radio Sens.*, **6**, 4563–4581, doi:[10.3390/rs6054563](https://doi.org/10.3390/rs6054563).
- Yang, W., H. Meng, R. R. Ferraro, I. Moradi, and C. Devaraj, 2013: Cross-scan asymmetry of AMSU-A window channels: Characterization, correction, and verification. *IEEE Trans. Geosci. Remote Sens.*, **51**, 1514–1530, doi:[10.1109/TGRS.2012.2211884](https://doi.org/10.1109/TGRS.2012.2211884).
- You, Y., and G. Liu, 2012: The relationship between surface rainrate and water paths and its implications to satellite rainrate retrieval. *J. Geophys. Res.*, **117**, D13207, doi:[10.1029/2012JD017662](https://doi.org/10.1029/2012JD017662).
- , —, Y. Wang, and J. Cao, 2011: On the sensitivity of Tropical Rainfall Measuring Mission (TRMM) Microwave Imager channels to overland rainfall. *J. Geophys. Res.*, **116**, D12203, doi:[10.1029/2010JD015345](https://doi.org/10.1029/2010JD015345).
- , F. J. Turk, Z. S. Haddad, L. Li, and G. Liu, 2014: Principal components of multifrequency microwave land surface emissivities. Part II: Effects of previous-time precipitation. *J. Hydrometeorol.*, **15**, 20–37, doi:[10.1175/JHM-D-13-07.1](https://doi.org/10.1175/JHM-D-13-07.1).
- , N.-Y. Wang, and R. Ferraro, 2015: A prototype precipitation retrieval algorithm over land using passive microwave observations stratified by surface condition and precipitation

- vertical structure. *J. Geophys. Res. Atmos.*, **120**, 5295–5315, doi:[10.1002/2014JD022534](https://doi.org/10.1002/2014JD022534).
- , —, —, and P. Meyers, 2016a: A prototype precipitation retrieval algorithm over land for ATMS. *J. Hydrometeor.*, **17**, 1601–1621, doi:[10.1175/JHM-D-15-0163.1](https://doi.org/10.1175/JHM-D-15-0163.1).
- , —, —, and S. Rudlosky, 2016b: Quantifying the snowfall detection performance of the GPM Microwave Imager channels over land. *J. Hydrometeor.*, **18**, 729–751, doi:[10.1175/JHM-D-16-0190.1](https://doi.org/10.1175/JHM-D-16-0190.1).
- Zhang, J., Y. Qi, C. Langston, and B. Kaney, 2011: Radar Quality Index (RQI)—A combined measure for beam blockage and VPR effects in a national network. *IAHS Publ.*, **351**, 388–393.
- , and Coauthors, 2016: Multi-Radar Multi-Sensor (MRMS) quantitative precipitation estimation: Initial operating capabilities. *Bull. Amer. Meteor. Soc.*, **97**, 621–638, doi:[10.1175/BAMS-D-14-00174.1](https://doi.org/10.1175/BAMS-D-14-00174.1).